Analysis and Optimization Study of Shrouded Horizontal Axis Wind Turbines

Tariq Abdulsalam Khamlaj

Supervision:
Dr. Markus Peer Rumpfkeil

Department of Mechanical and Aerospace Engineering

January 9, 2018

Introduction

- The emissions of gases that arise from burning massive quantities of fossil fuels for power production worldwide cause numerous environmental issues such as smog, acid rain, as well as climate change.
- In recent years, there have been large global efforts to reduce the dependence on fossil fuels by investing more in renewable energy technologies such as wind energy.
- However, the scale of wind power usage is still small in comparison with the overall demand for energy.

Outline

1. Shrouded Wind Turbines
   - Effect of Shroud
   - History
   - Objective
2. Numerical Model
   - CFD solver
   - Empty Shroud
   - Wind Turbine Simulation Tool
   - Shrouded Wind Turbine
   - 3D Vs. Axisymmetric Actuator Disk
3. Shape Optimization Methodology
   - Optimization Framework
   - Case Setup
   - Sample Grid Convergence Study
4. Shape Optimization Results
5. Conclusion and Future Work

Effect of Shroud

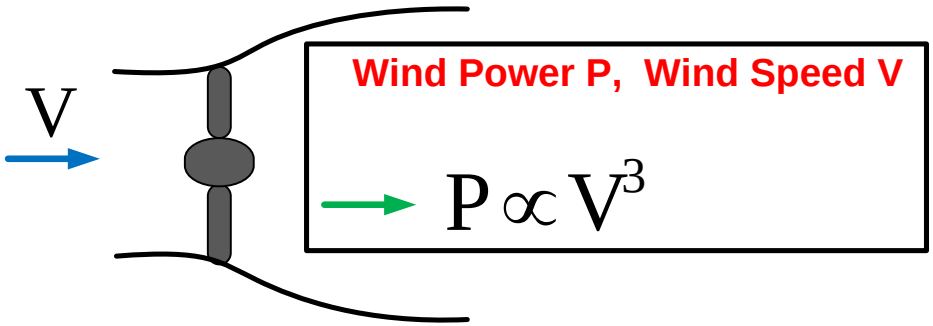

$$P = \frac{1}{2}\rho C_P A V^3$$

- Basic idea is to increase power output without necessarily increasing the size of the rotor.
- The concept of accelerating the wind is named the "Wind lens".

Wind Lens

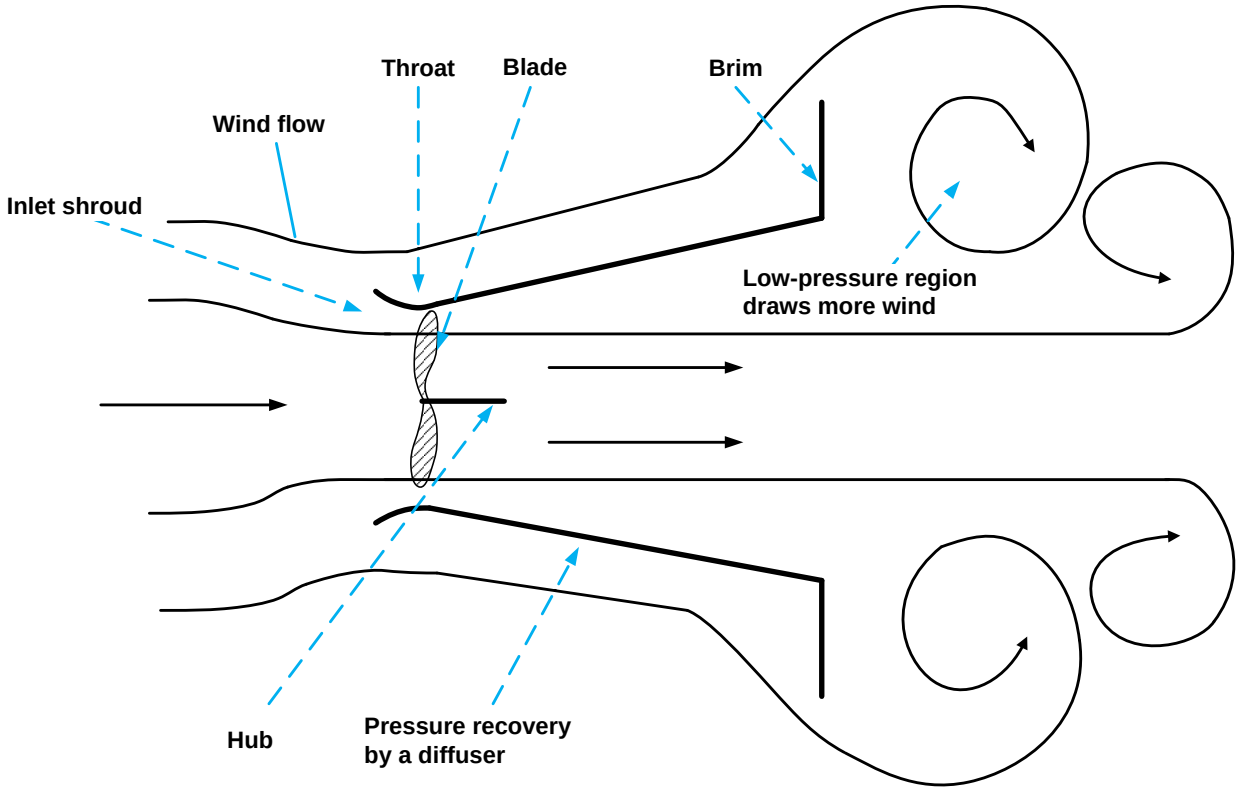

Figure 1 : Flow around and through wind turbine with brimmed diffuser (Wind-lens).

History I

- The first assessment on "ducted windmills" was performed by Lilley and Rainbird in 1956 [1].
- In the seventies, a significant amount of wind tunnel experiments were carried out by Foreman et al [2, 3] from Grumman Aerospace Dept. USA, and by Kogan, Seginer and Igra [4, 5].
- The Lilley and Rainbird study [1] concluded that no performance improvements were possible.
- Foreman et al [3] concluded that the DAWT can produce four times the power than a same-sized bare wind turbine.
- In 1979, a conclusion at the Wind Energy Innovative system Conference led to the disappearance of DAWT due to economical issues.

History II

- In 1997, a company called Vortec Energy Limited of New Zealand attempted to commercialize DAWT, but they have ceased trading.
- In 2004, group of researchers at Kyushu University have concluded a power factor increase by 4 times compared to a bare wind turbine and are trying to commercialize the DAWT.

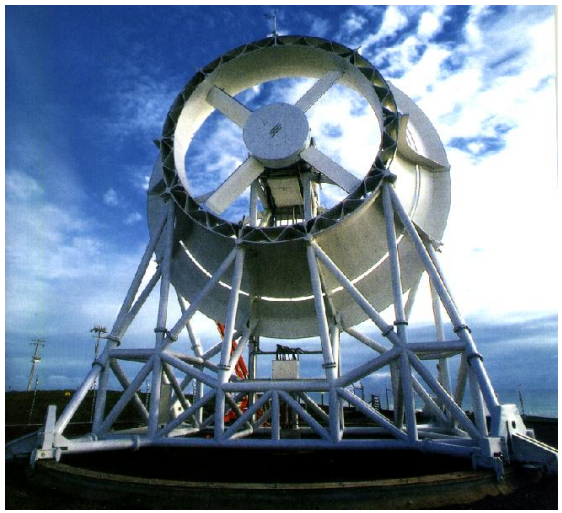

(a) Vortec Energy.

(b) DAWT.

Objective

- Shrouded wind turbines with a brimmed diffuser have demonstrated power augmentation by a factor of about 4 to 5 compared with a bare wind turbine, for a given turbine diameter and wind speed [6, 7].
- The objective of this research is to improve the wind-lens efficiency by designing the duct and brim shape through an optimization process that maximizes the power while minimizing drag for a given turbine rotor shape.

CFD solver

- The computational analysis is performed with the Open source Field Operation And Manipulation (OpenFoam) CFD code.
- The governing equations of the flow field solved by the simpleFoam solver are the steady state, incompressible form of the continuity and conservation of momentum equations.
- For the simulation of the effects of turbulence on the main flow, the *Spalart* – *Allmaras*, the $k-\epsilon$, and the $k-\omega$ Shear Stress Transport (SST) model are utilized.
- The computational meshes are generated using the open source tool Gmsh.

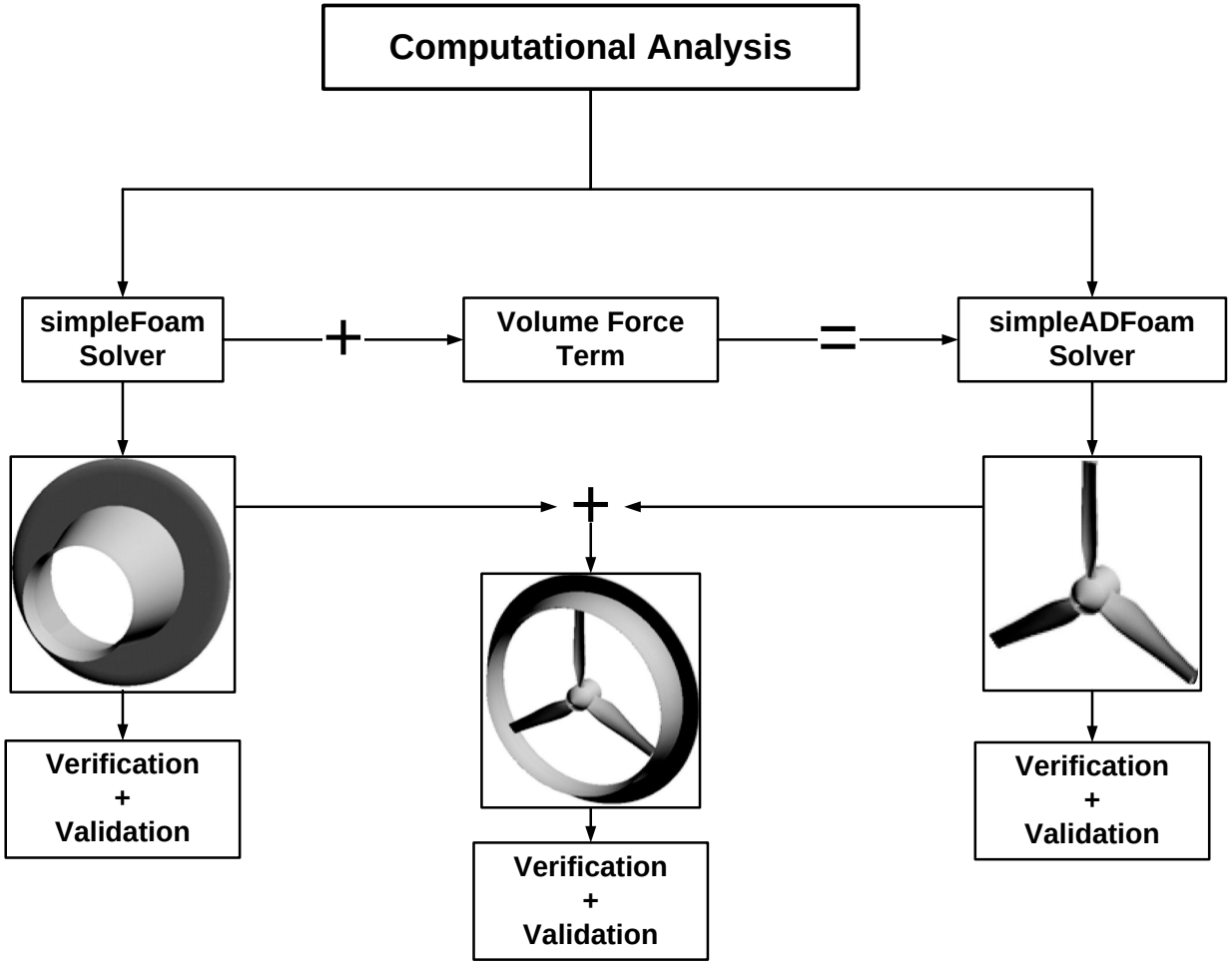
Computational Analysis
simpleFoam Solver
+
Volume Force Term
=
simpleADFoam Solver
+
Verification + Validation
Verification + Validation
Verification + Validation

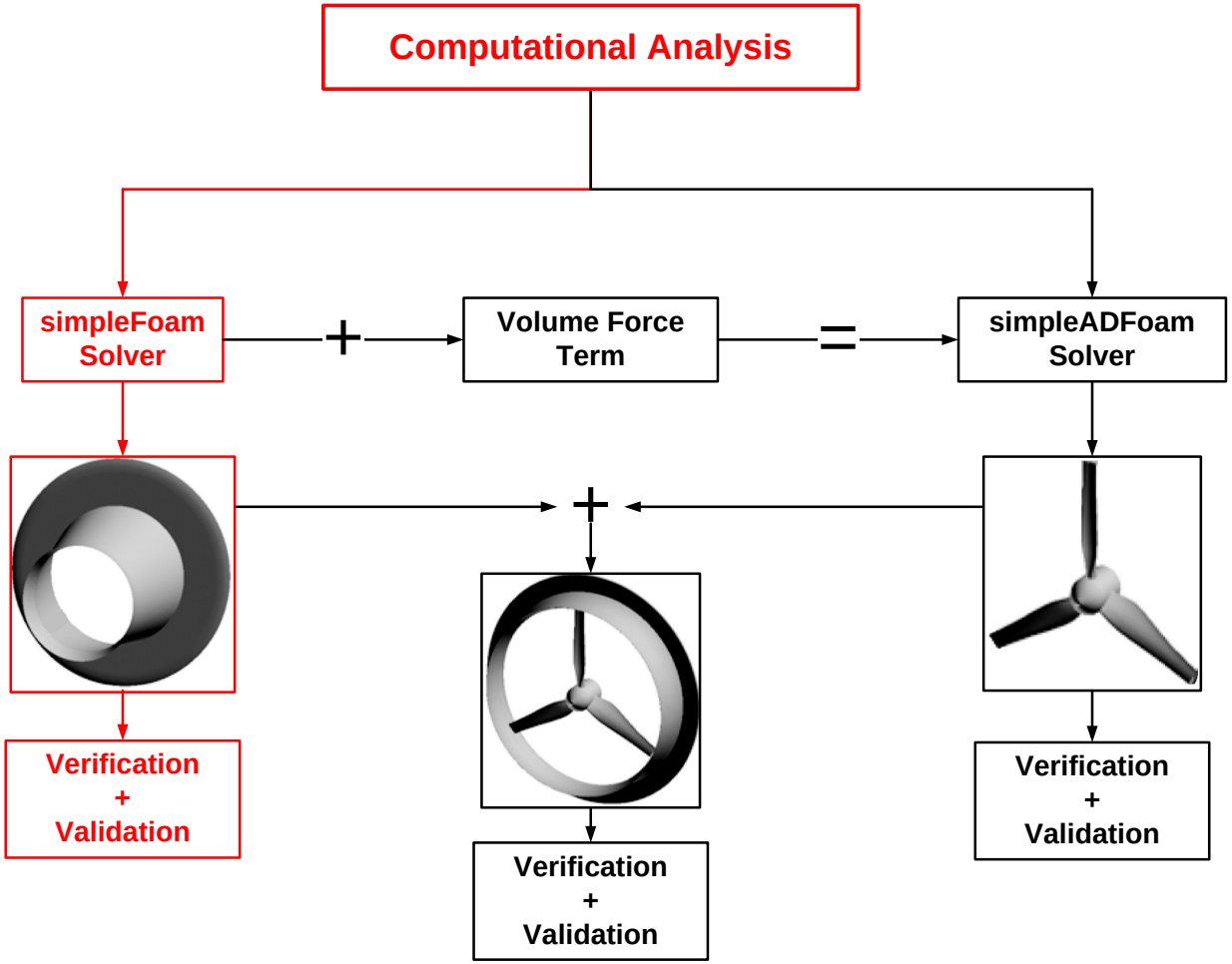
Computational Analysis
simpleFoam Solver
+
Volume Force Term
=
simpleADFoam Solver
Verification + Validation
Verification + Validation
Verification + Validation

Case Setup and Boundary Conditions

Table 1 : Detailed information for shrouded diffuser.

Experimental model	Long type [8]
Diameter of the throat D	600mm
Diameter of the hub D_h	0.22D
Height of the flange h	0.5D
Diffuser length L_D	1.25D
Inlet length L_N	0.25D
Tip clearance	10 mm
Semi-open angle θ	12^o
Inlet velocity V_∞	6 m/s

Table 2 : Fluid Properties.

Property	Value
Kinematic Viscosity ν	$1.5 \times 10^{-5} m^2/s^2$
Air Density ρ	$1.225 kg/m^3$
Reynolds No. Re	$2.2 \times 10^5 - 5.5 \times 10^5$

Table 3 : Pertinent discretization information.

Aspect	Description
Coordinates system	3-D
Computational grid	H-O type
Scheme	Finite volume method
Coupling algorithm	SIMPLE method
Laplacian schemes	Gauss limitedLinear
Gradient schemes	cellLimited $<$ *gradScheme* $>$
Divergence schemes	upwind

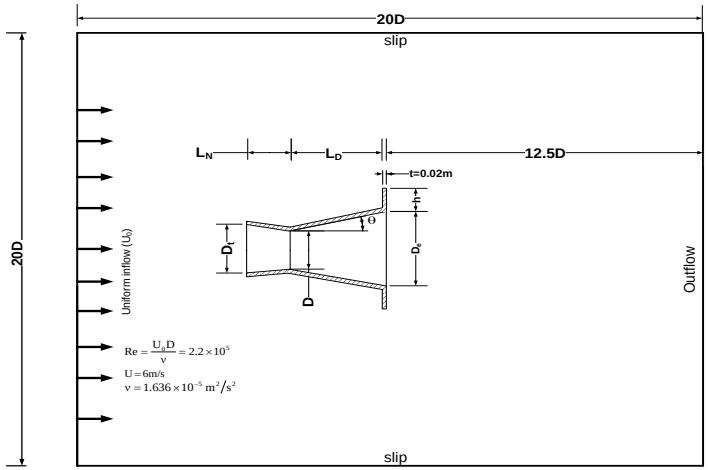

Figure 2 : Computational domain and BCs.

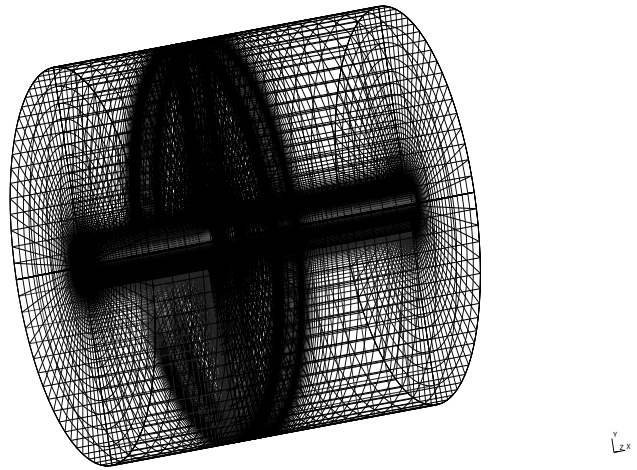

Figure 3 : Example for the 3D grid.

Grid Independence Study I

- Computational field: Cylindrical shape (length = 20D, Diameter=20D)
- The fluid is set to be air at a temperature of $25^{\circ}C$.
- The reference pressure is 1atm.
- Inlet (velocity inlet): 6m/s.
- Outlet (pressure outlet): 0Pa
- Domain walls: free slip wall
- Diffuser walls: no slip walls

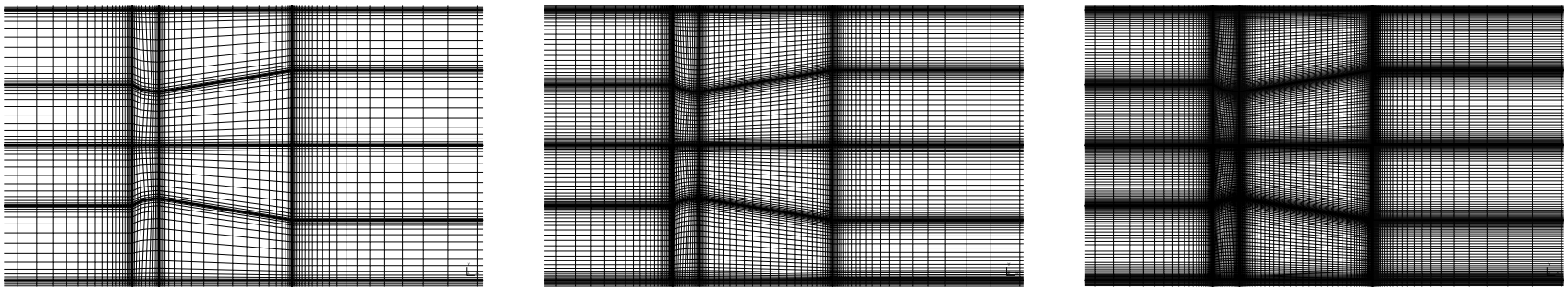

(a) No. of nodes 75672. (b) No. of nodes 116208. (c) No. of nodes 180384.

Figure 4 : Grids used with $k - \epsilon$ turbulence model for the grid independence study.

Grid Independence Study II

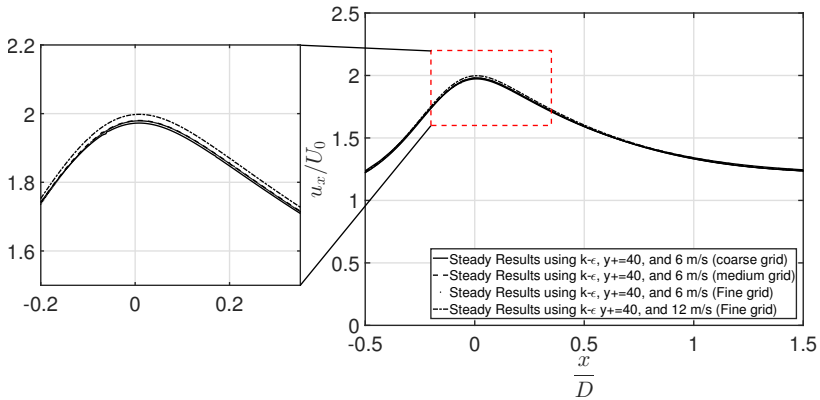

(a) Velocity distribution.

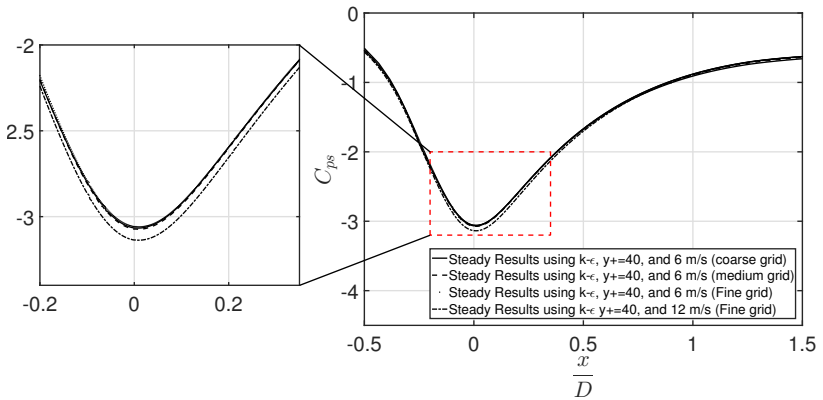

(b) Pressure distribution.

Figure 5 : Velocity and pressure distribution for the three grids with $k - \epsilon$ turbulence model.

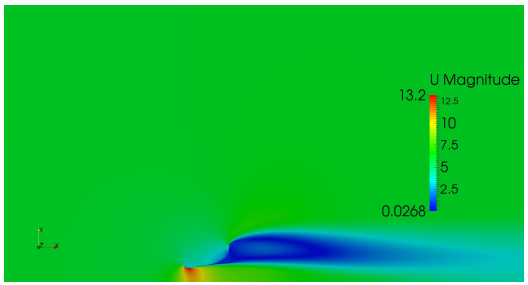

(a) V dist. using $k - \omega$.

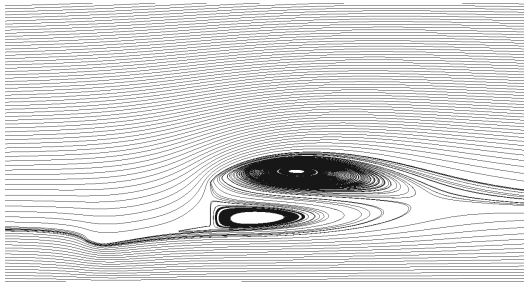

(b) Streamlines using $k - \omega$.

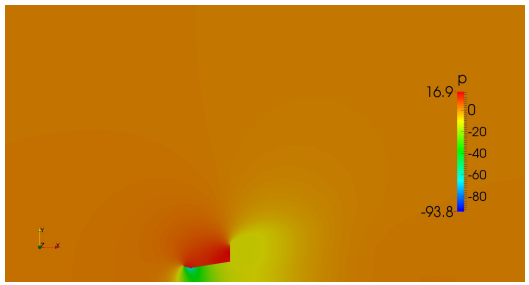

(c) P dist. using $k - \omega$.

Effect of Turbulence Models

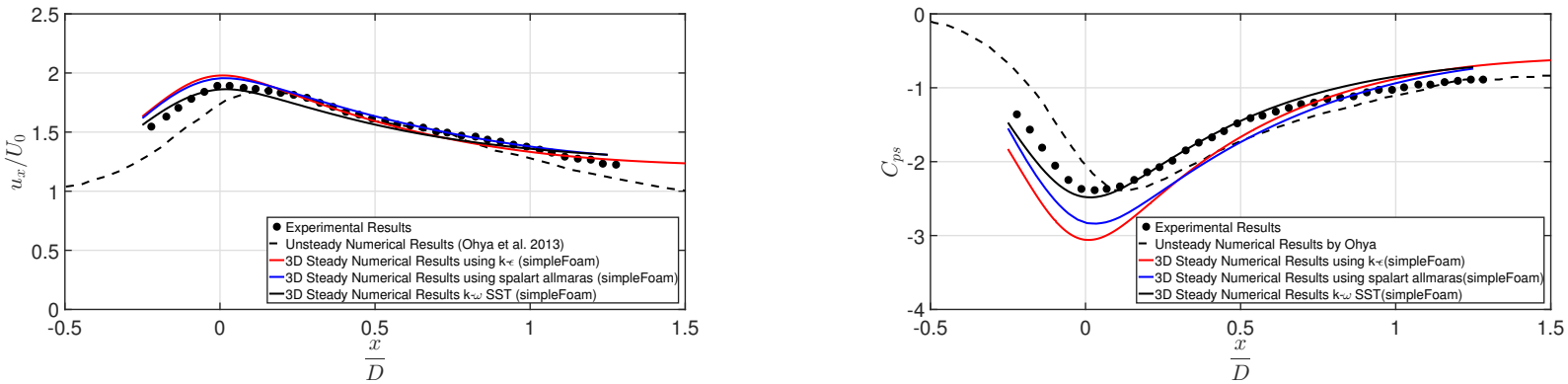

(a) Velocity distribution.

(b) Pressure distribution.

Figure 7 : Velocity and pressure distribution through an empty flanged diffuser using different turbulence models.

Conclusion

Even though the $k-\omega$ (SST) turbulence model results are in best agreement due to its ability to model boundary layer separation in adverse pressure gradients, it is not always practical to mesh down to $y^+ \simeq 1$ wall spacings when considering the overall computational cost required to search for an optimized shrouded design in the preliminary design stage. Therefore, the $k-\epsilon$ with standard wall functions is chosen.

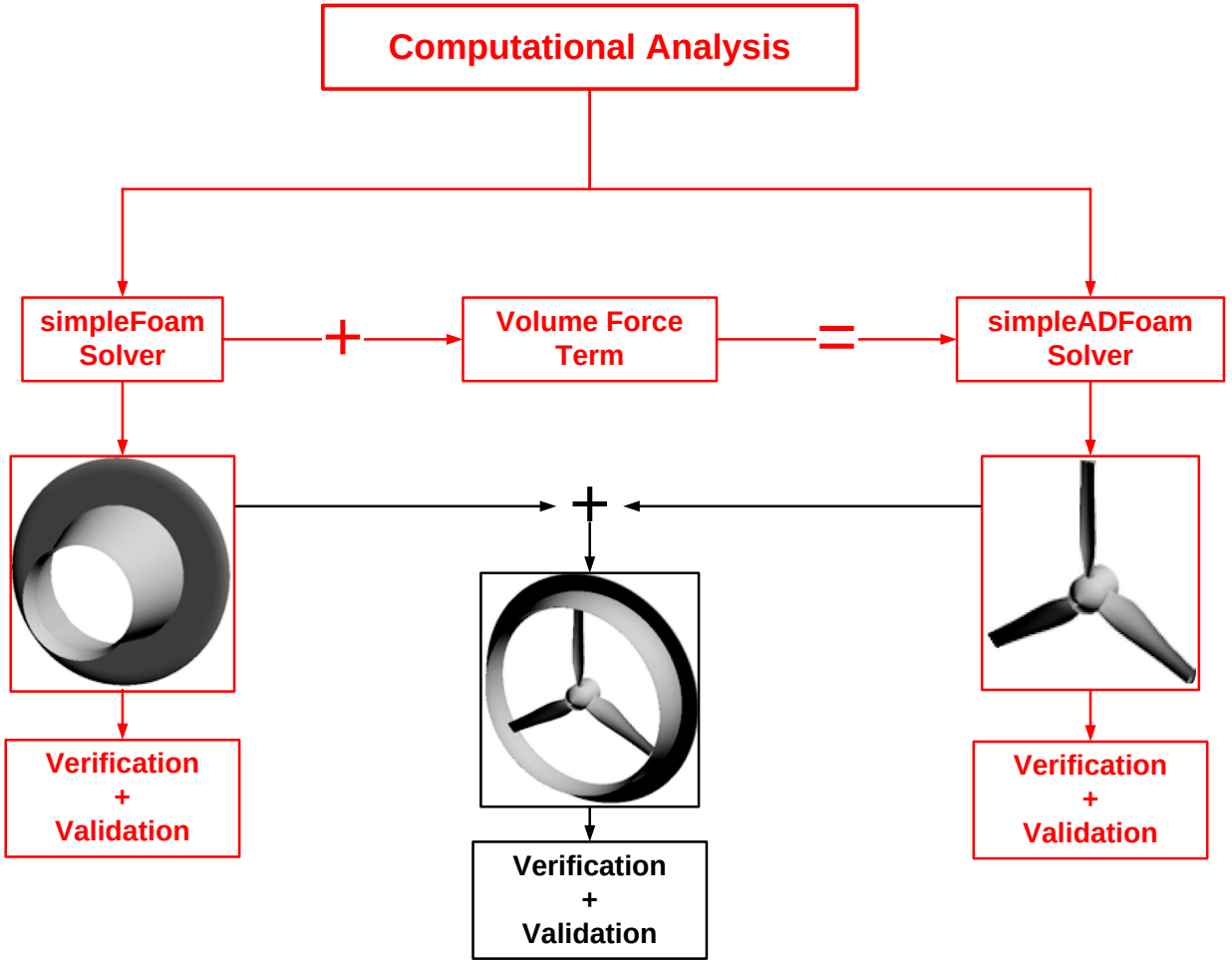
Computational Analysis
simpleFoam Solver
+
Volume Force Term
=
simpleADFoam Solver
Verification + Validation
Verification + Validation
Verification + Validation

Analysis of Wind Turbine

- Wind turbine aerodynamic simulations are important for developing future wind turbines.
- Three main methods of analysis are available:
  - Actuator Disk (AD) coupled with Blade Element Method (BEM).
  - Actuator Line (AL).
  - Fully resolved blade profile model (FR).

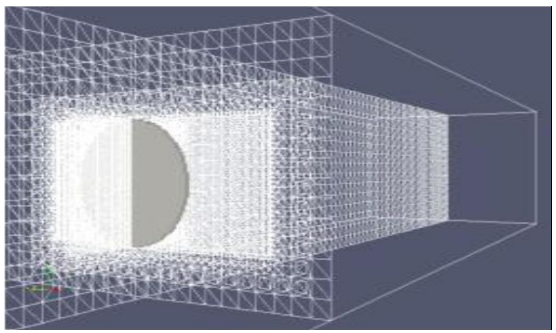

(a) AD.

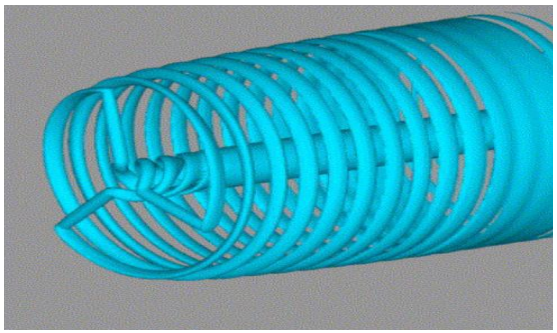

(b) AL [9].

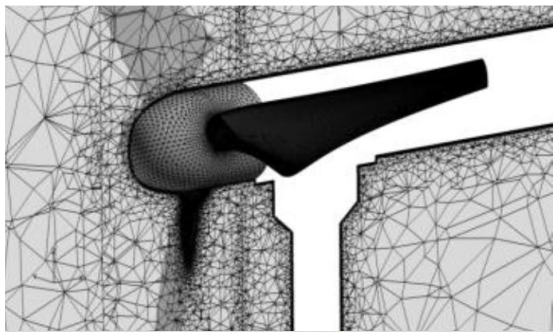

(c) FR [9].

Analysis of Wind Turbine

	Advantages	Disadvantages
AD+BEM	• Simple model. • Very low computational cost.	• Cannot reproduce detailed wake structure. • Input parameters are difficult to handle. • Need to rely on tabulated airfoil data.
AL	• Can potentially reproduce detailed wake structure. • Low computational cost.	• Input parameters are difficult to handle. • Need to rely on tabulated airfoil data.
FR	• Best Model in wake reproduction. • Does not rely on tabulated airfoil data.	• Very high computational cost and large meshing effort.

Governing Equations for BEM Used with AD Model

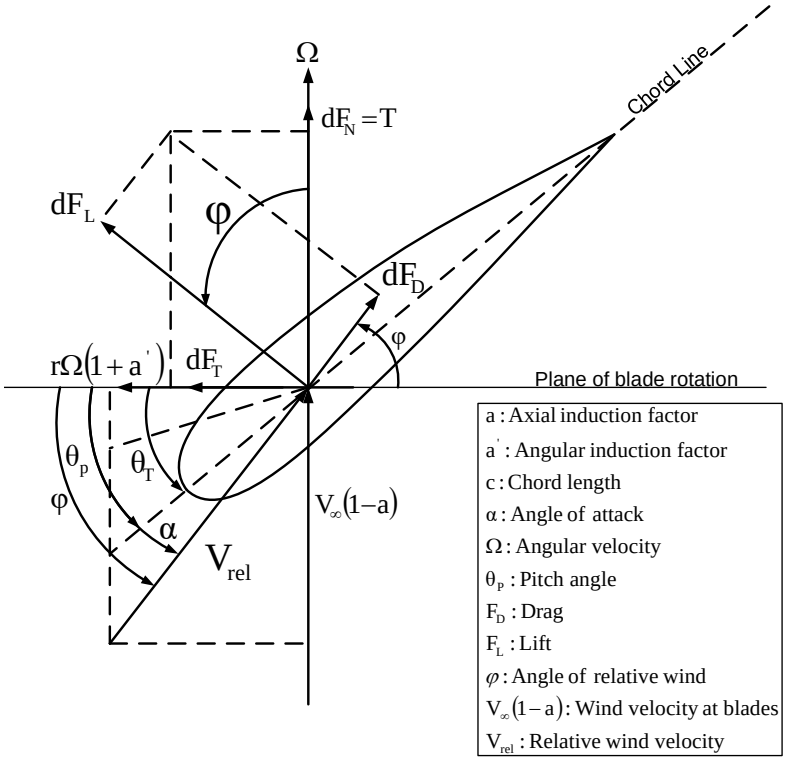

(a) F_L and F_D acting on a blade [10].

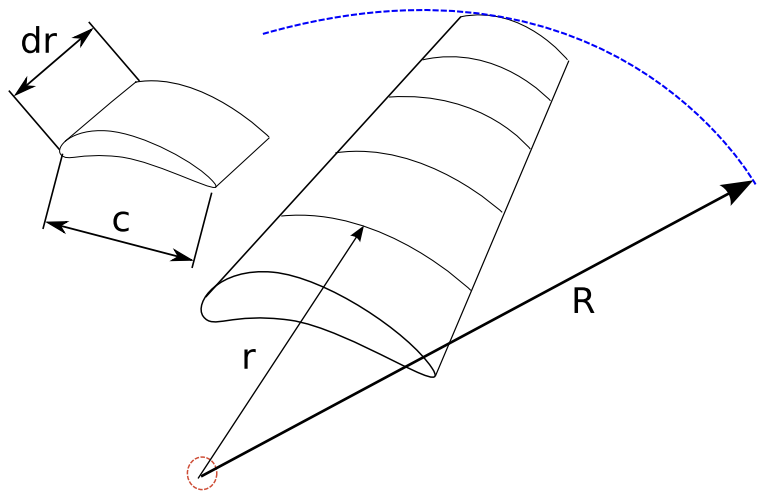

(b) Schematic of blade elements [11].

Figure 8 : Blade geometry for analysis of a horizontal axis wind turbine.

Governing Equations for BEM Used with AD Model

Blade element theory relies on two key assumptions:

- There are no aerodynamic interactions between different blade elements.
- The forces on the blade elements are solely determined by the lift and drag coefficients.

The incompressible (RANS) equations are taken as the governing flow equations.

- The continuity equation:

$$\frac{\partial \overline{u}_i}{\partial x_i} = 0 \tag{1}$$

- The momentum equation:

$$\overline{u}_j \frac{\partial \overline{u}_i}{\partial x_j} = -\frac{1}{\rho}\frac{\partial \overline{p}}{\partial x_i} + \nu \frac{\partial^2 \overline{u}_i}{\partial x_j^2} - \frac{\partial \overline{u_i' u_j'}}{\partial x_j} + \frac{\vec{S}_{AD}}{\rho} \tag{2}$$

Verification and Validation of the Solver I

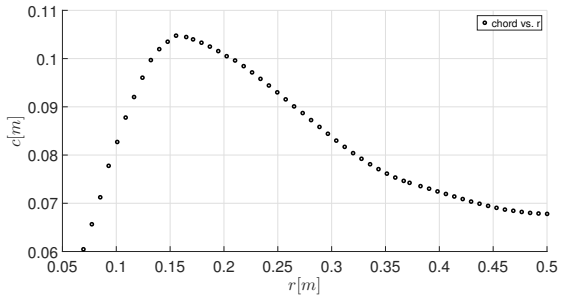

(a) Chord distribution.

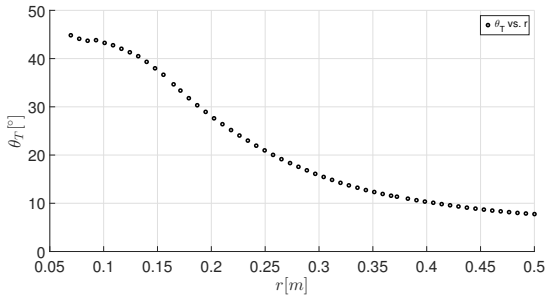

(b) Twist distribution.

Figure 9 : Chord and twist distribution of the blade given in table 4.

Table 4 : Airfoils along blade used in Ohya et al.[7, 8].

Radius	Airfoil Type
69.5mm	MEL20
357.0mm	MEL18
500.0mm	MEL12

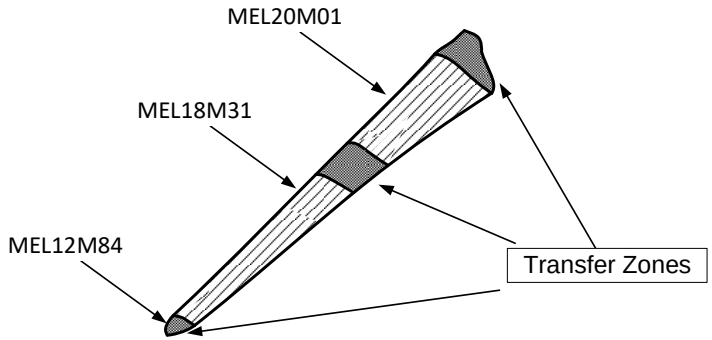

Figure 10 : Schematic diagram of the blade.

Verification and Validation of the Solver II

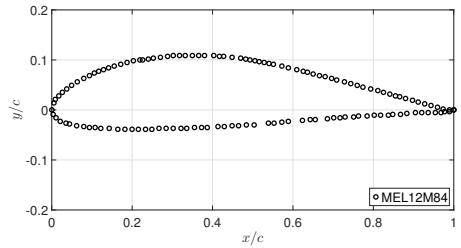

(a) MEL12M84.

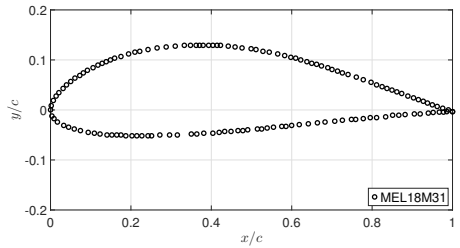

(b) MEL18M31.

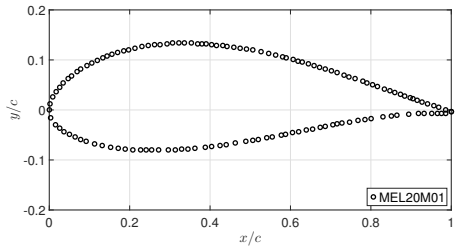

(c) MEL20M01.

Figure 11 : MEL airfoil series used in the blade [12].

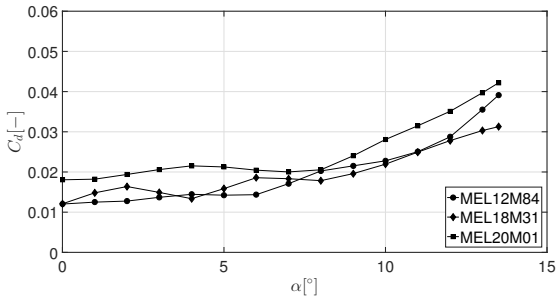

(a) Cd vs α distribution.

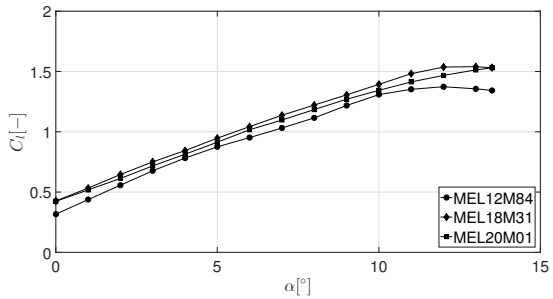

(b) Cl vs α distribution.

Figure 12 : Experimental lift and drag coefficients vs. angle of attack of each airfoil used in the blade [8].

Verification and Validation of the Solver III

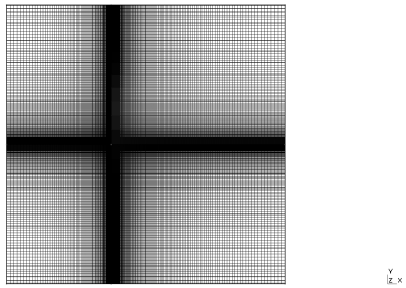

(a) Side view of the coarse grid.

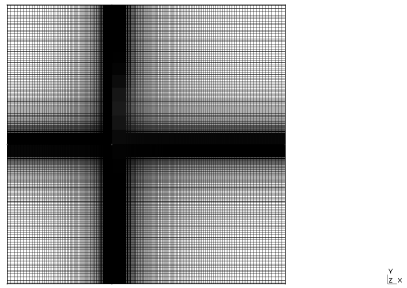

(b) Side view of the medium grid.

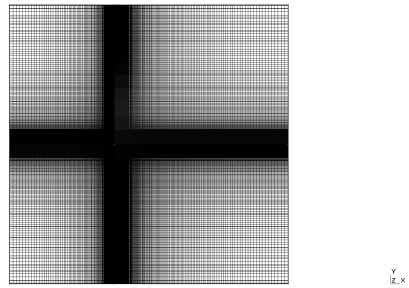

(c) Side view of the fine grid.

Figure 13 : Grids employed for the grid dependence study.

Table 5 : Results of three selected grids for tip speed $\lambda = 3.5$.

N_{nodes}	**Thrust [N]**	**Torque [N.m]**
148800	18.4465	1.80107
312768	18.1198	1.78795
536272	17.8072	1.77792

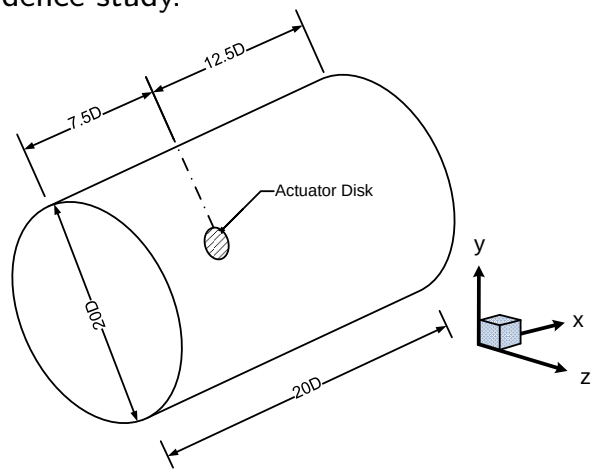

Figure 14 : Far-field domain used for simulation.

Verification and Validation of the Solver IV

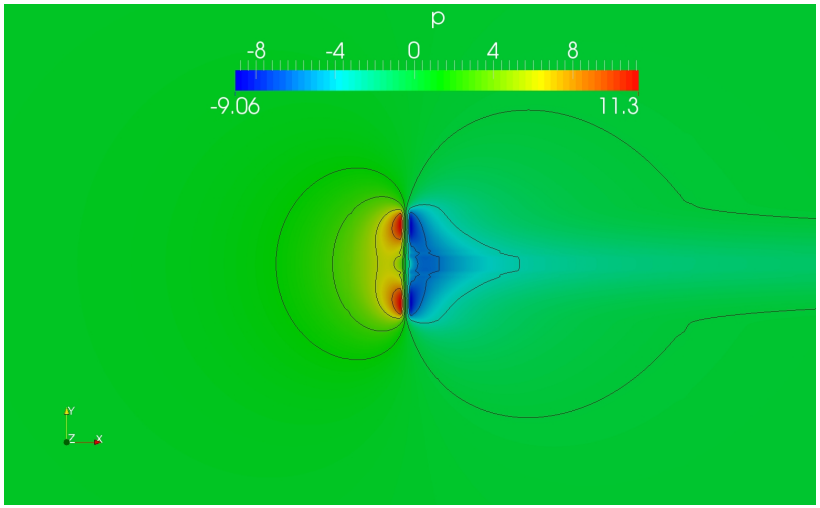

(a) Pressure distribution on the fine grid.

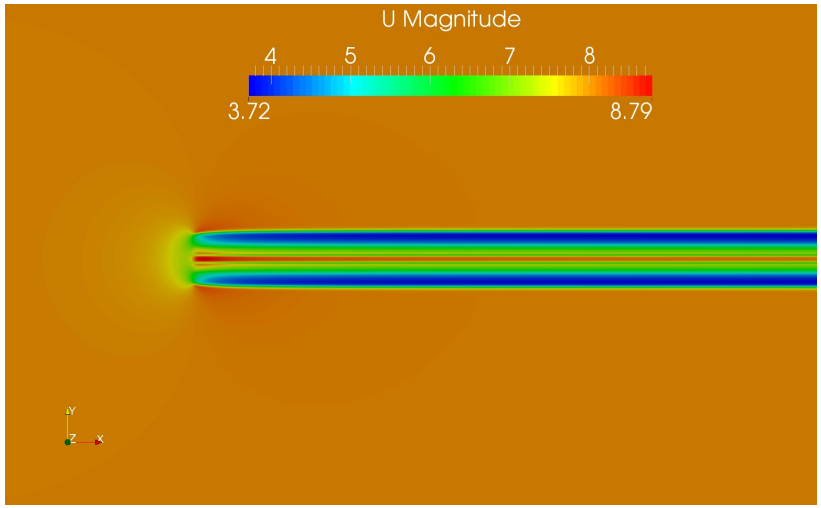

(b) Velocity distribution on the fine grid.

Figure 15 : Velocity and pressure distribution of the three grids for tip speed $\lambda = 3.5$.

Verification and Validation of the Solver V

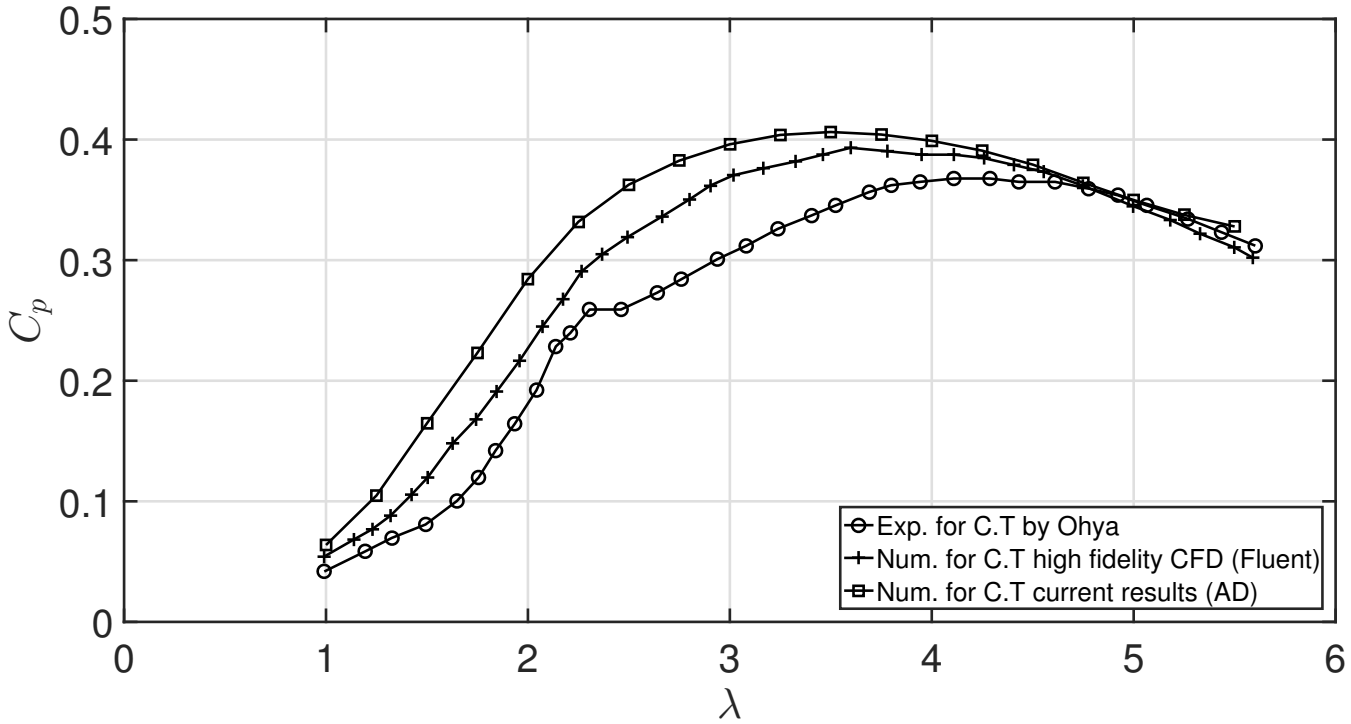

Figure 16 : Validation study of the power coefficients vs. tip speed [7, 8].

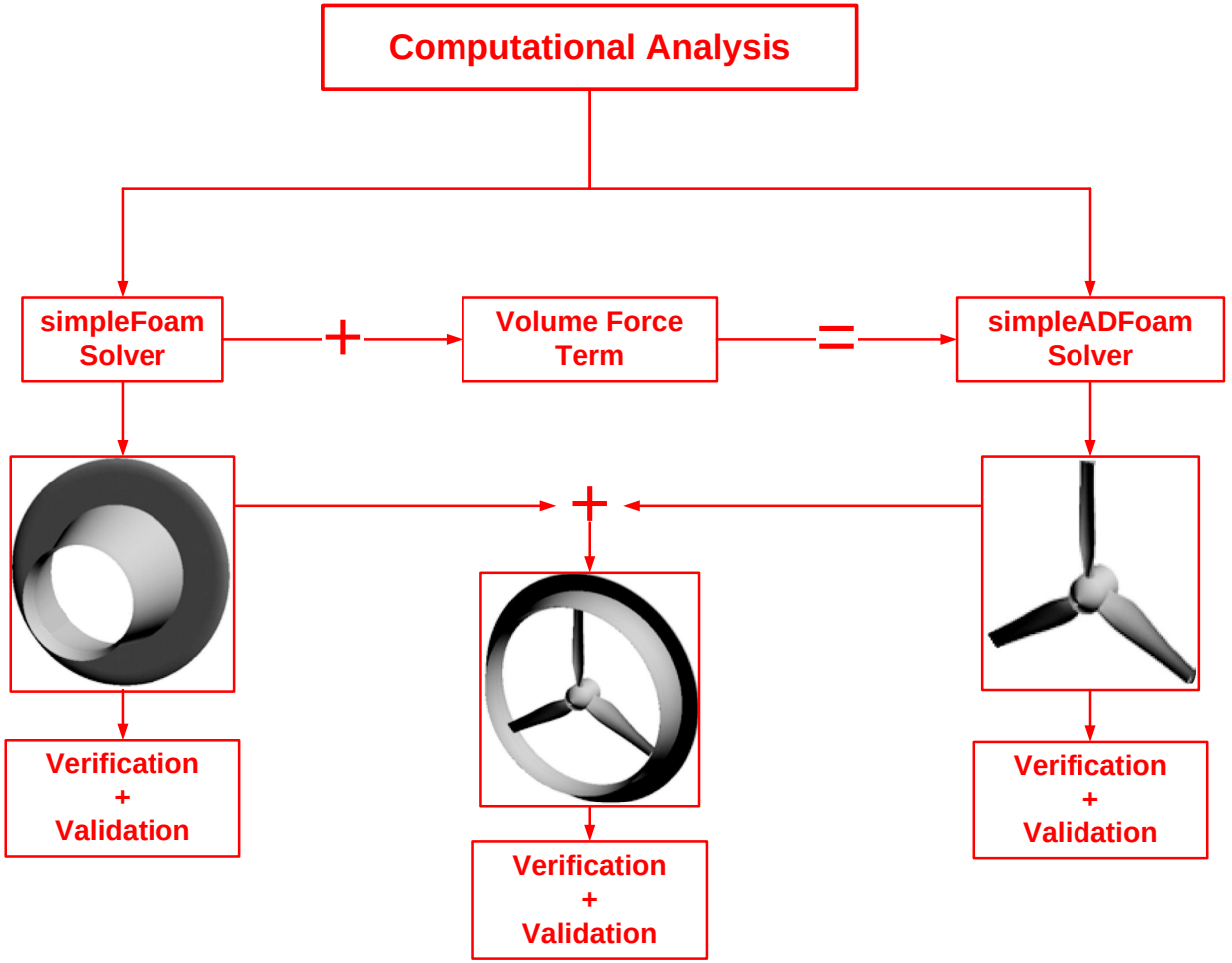
Computational Analysis
simpleFoam Solver
+
Volume Force Term
=
simpleADFoam Solver
Verification + Validation
+
Verification + Validation
Verification + Validation

Full Configuration I

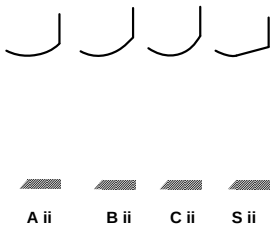

Figure 17 : Sectional shapes of wind-lenses used by Ohya et al.[7].

Table 6 : Parameters for wind-lens shapes by Ohya et al.[7].

Diffuser	A ii	B ii	C ii	S ii
$(L_D + L_N)/D$	0.225	0.221	0.221	0.225
A_{exit}/A_{throat}	1.173	1.288	1.294	1.119

Table 7 : Detailed information for Sii-types wind-lens.

Experimental model	Compact Sii type
Diameter of the throat D	1020mm
Diameter of the hub D_h	0.13D
Height of the flange h	0.1D
Diffuser length L_D	0.137D
Inlet length L_N	0.088D
Tip clearance	10 mm
Semi-open angle θ	12^o
Inlet velocity V_∞	8 m/s

Full Configuration II

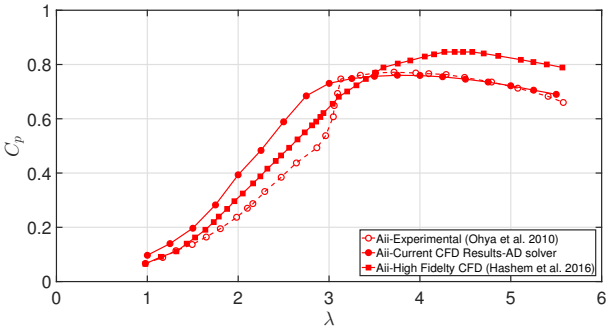

(a) *Aii* Type.

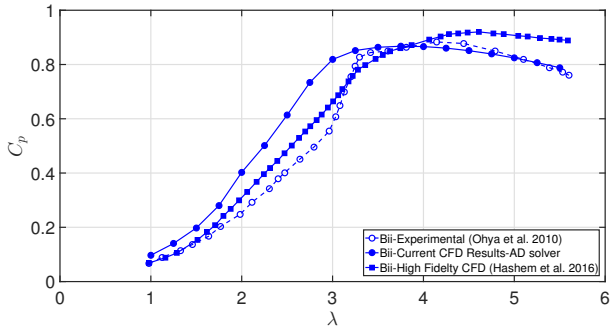

(b) *Bii* Type.

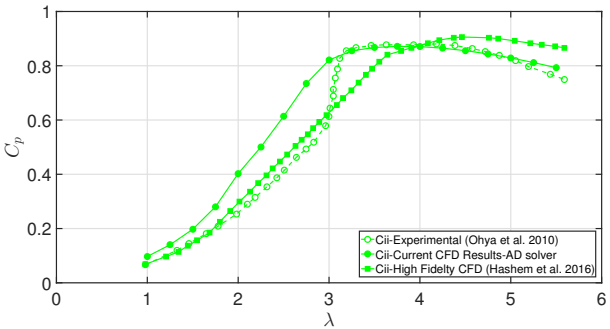

(c) *Cii* Type.

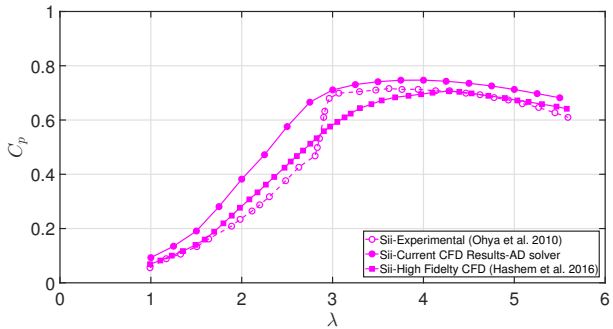

(d) *Sii* Type.

Figure 18 : Comparisons among low- and high-fidelity CFD results as well as experimental data.

3D Vs. Axisymmetric Actuator Disk

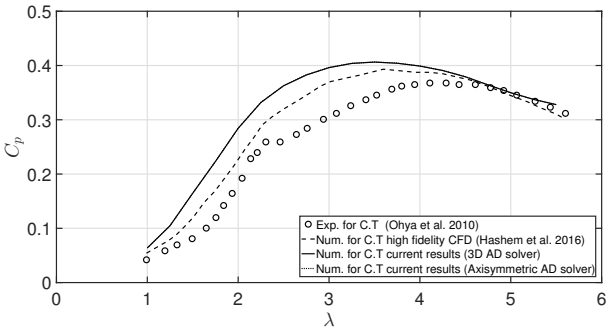

(a) Conventional turbine.

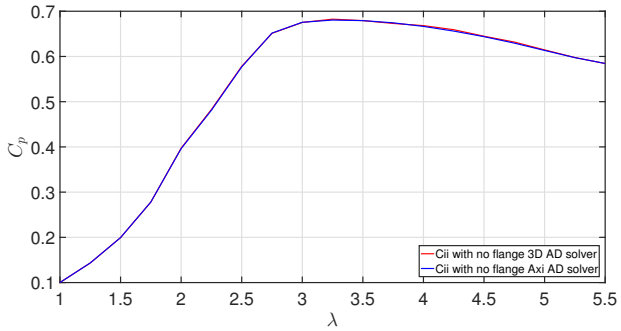

(b) Shrouded turbine.

Figure 19 : Verification of the axisymmetric implementation in comparison to full 3D and literature results.

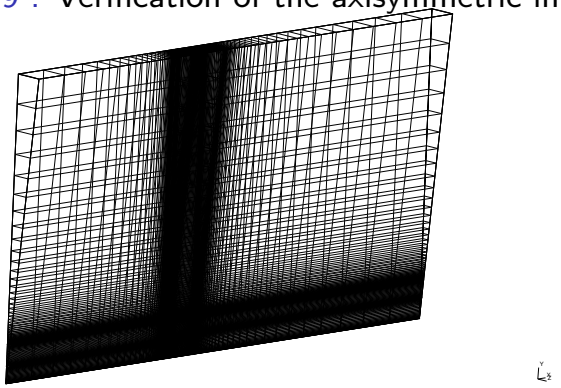

Figure 20 : Example of the axisymmetric grid.

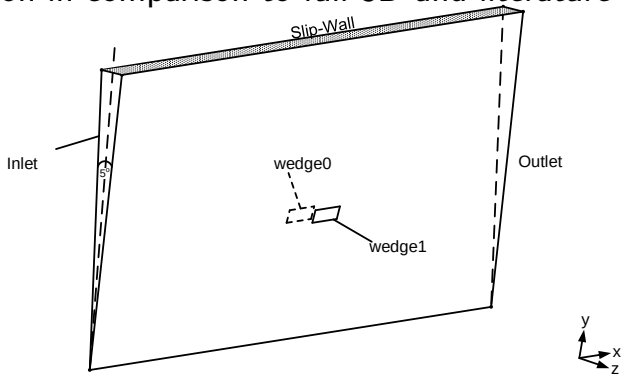

Figure 21 : Wedge boundary condition.

Optimization Algorithm

- One popular approach for optimization processes is evolutionary algorithms specifically, the use of Genetic Algorithms (GAs).
- GAs are semi-stochastic semi-deterministic optimization methods presented as natural evolution.
- GAs are based on the evaluation of a set of solutions (population).
- Random operations of selection, crossover and mutation are applied to the population.
- The probability of survival of new individuals relies on their fitness: the best are kept with a high probability, the worst are rapidly discarded [13].
- In this work, the software package DAKOTA with MOGA (Multi-Objective Genetic Algorithm) [14] is employed.

Why is a derivative-free global optimization method chosen?

This multi-objective shape optimization problem exhibits multimodal behavior and we do not have adjoint gradients available.

Shape Parameterization

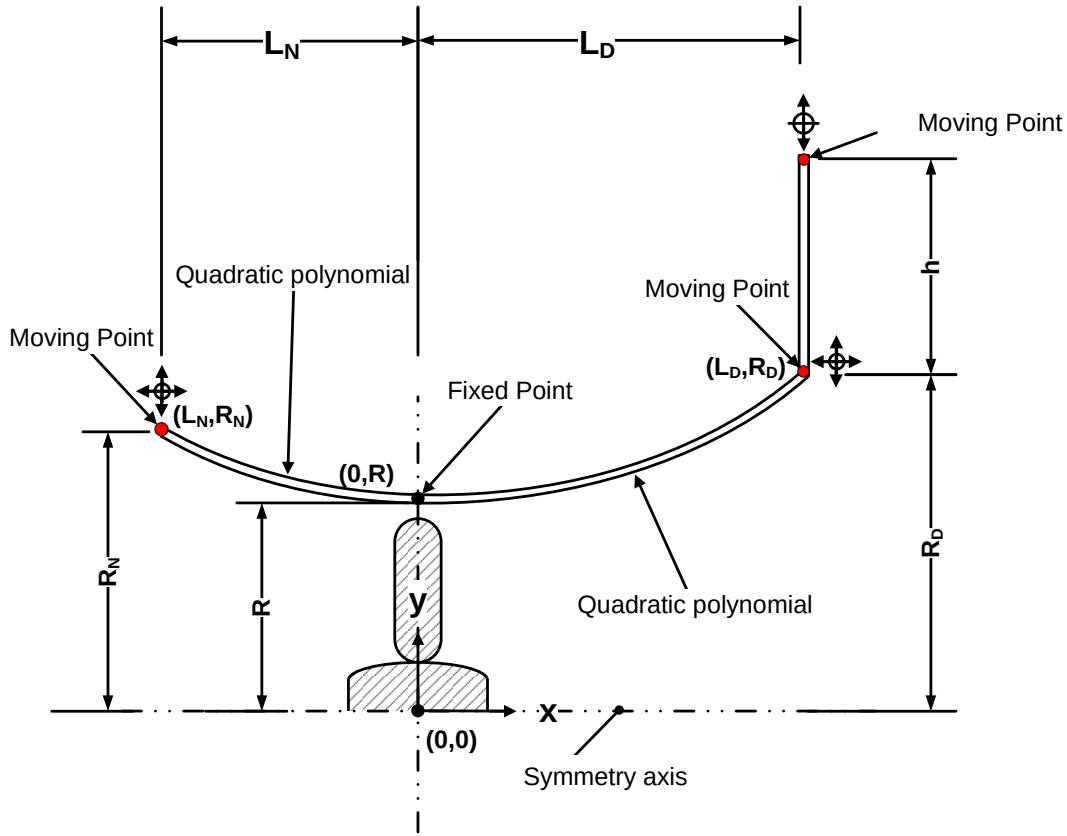

Figure 22 : Five design variables for the parameterization.

Objective Functions

- This work focuses on the shape optimization of the wind-lens for a given wind turbine rotor in order to maximize the power coefficient, C_P, subject to a drag constraint.
- The power coefficient, C_P, of the turbine is determined by integrating the radial and tangential forces over the blade.
- The drag coefficient, $C_d = \dfrac{F_d}{0.5\rho V_\infty^2 A_{brim}}$, is calculated using the force function in **OpenFOAM**.

Summary

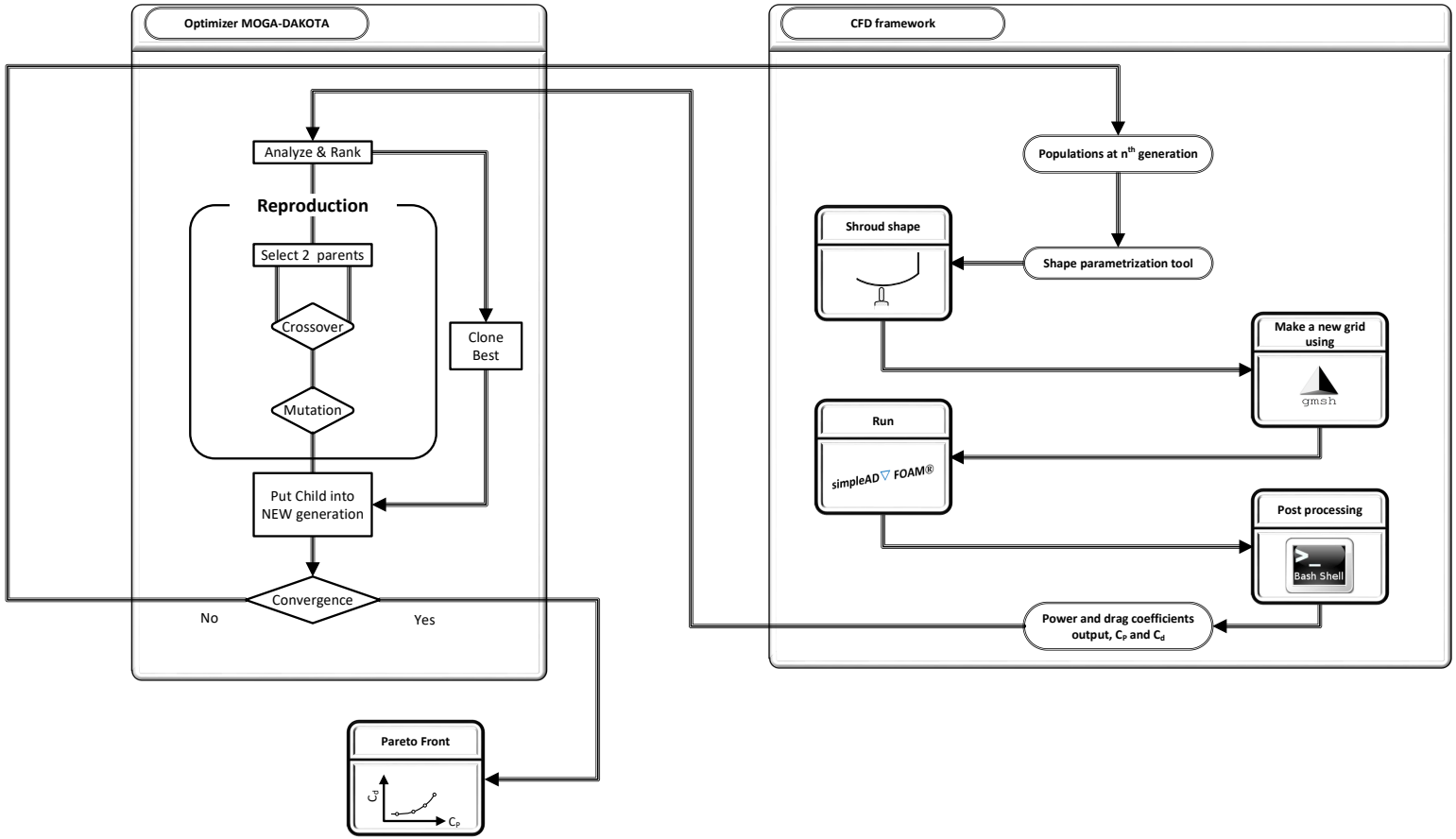

Figure 23 : Flow chart of the optimization approach.

Case Setup I

Table 8 : Conditions employed for all designs in the optimization process.

Parameter	Value
Number of blades N	3
Rotational Speed Ω	535 rpm
Tip speed ratio λ	3.5
Rotor tip radius R_{tip}	0.5 m
Hub radius R_{hub}	0.065 m
Rotor tip clearance	10 mm
Velocity inlet	8 m/s
Blade element profile	MEL12, MEL18, and MEL20

- Computational domain: Axisymmetric (length = 20D, Diameter=10D)
- Fluid is set to be air at a temperature of $25^{\circ}C$.
- Reference pressure: 1 atm.
- Turbulent inflow: $I_0 = 3.1\%$, $k_0 = 0.09m^2/s^2$ and $\epsilon_0 = 0.063m^2$
- Pressure outlet: 0 Pa
- Domain walls: free slip wall
- Diffuser walls: no slip walls with $k_{wall} = \epsilon_{wall} = 0$.

Case Setup II

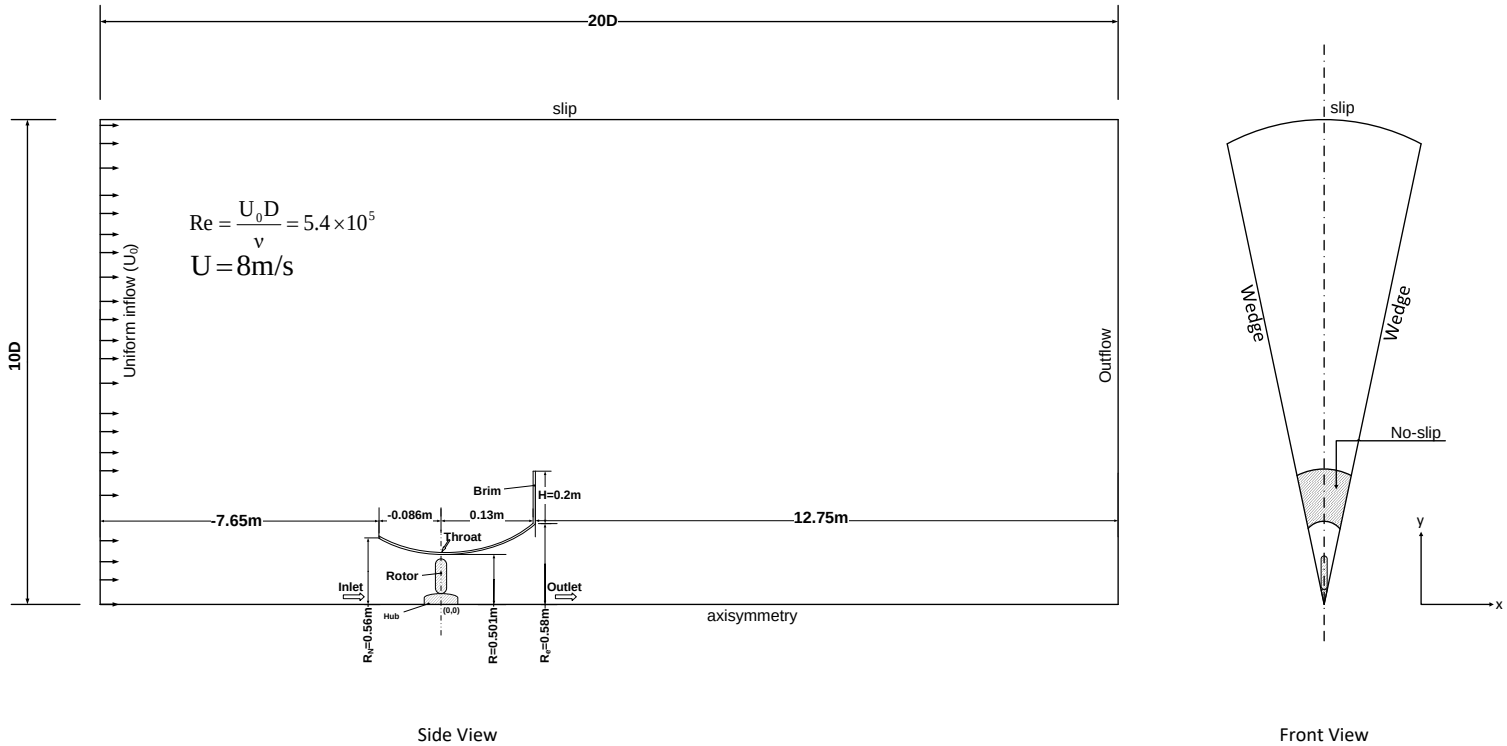

Figure 24 : CFD domain used for simulation.

Case Setup III

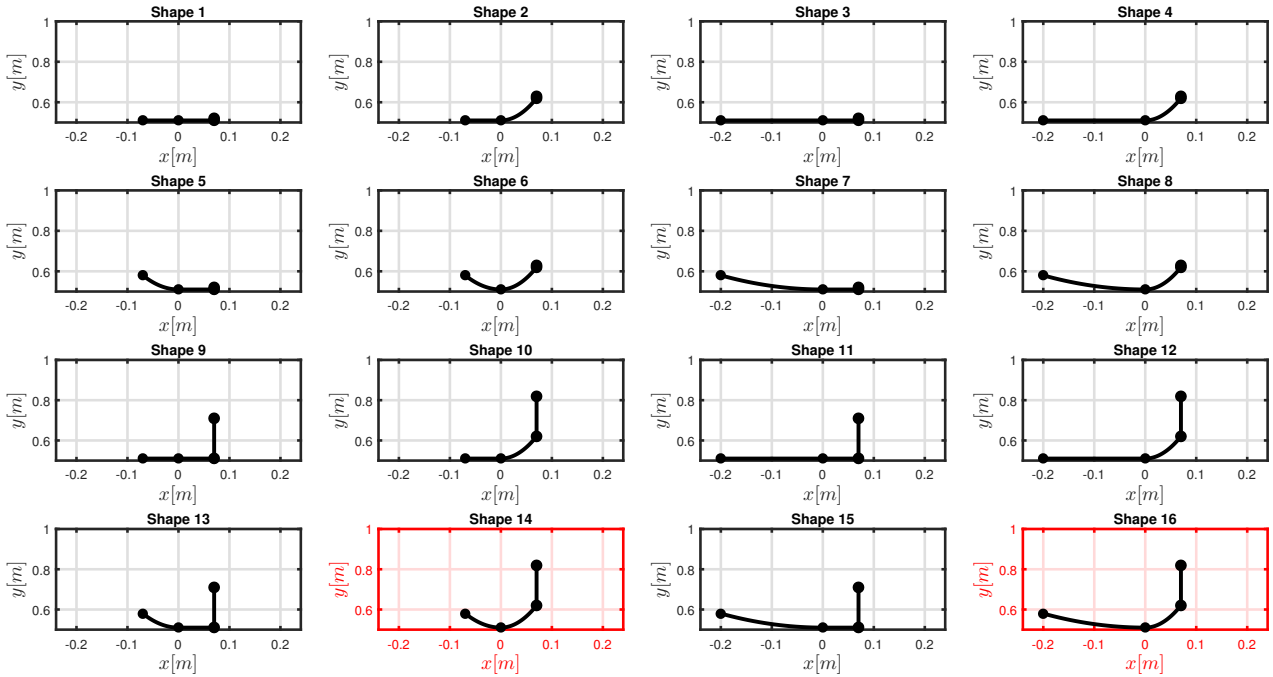

(a) First set of corners.

Figure 25 : $2^5 = 32$ extreme shapes in design space.

Case Setup IV

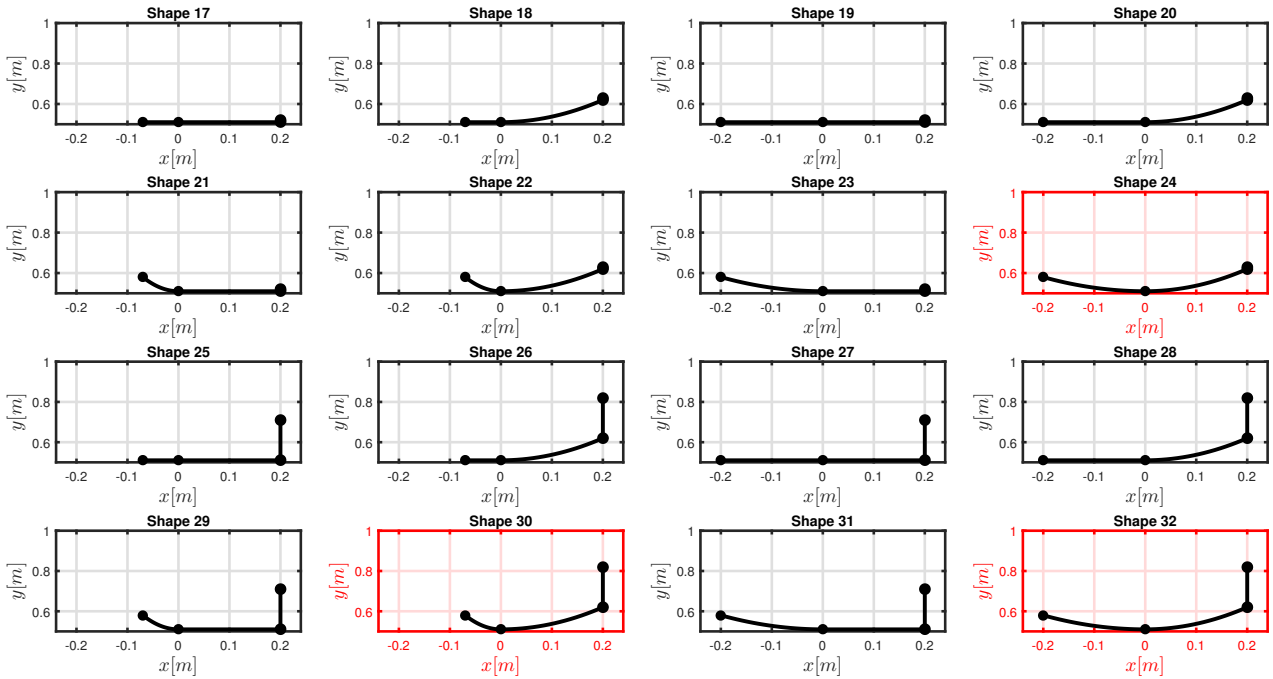

(b) Second set of corners.

Figure 25 : *Cont.*

Sample Grid Convergence Study

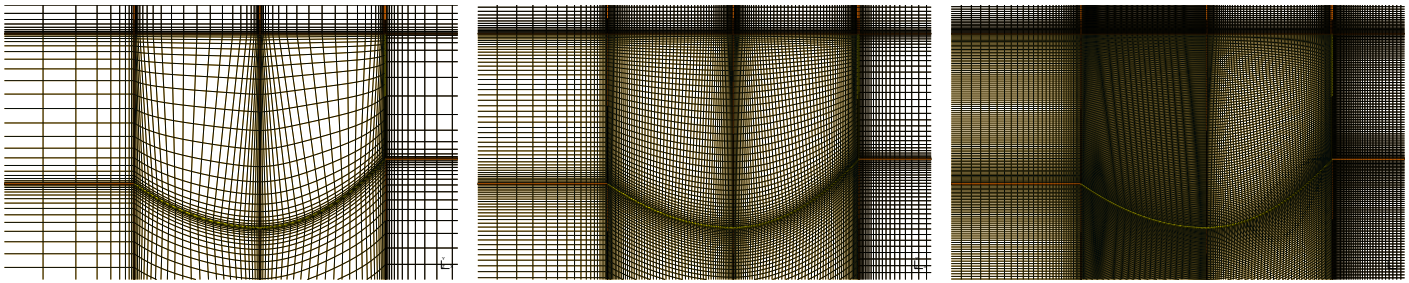

(a) Coarse Grid. (b) Medium Grid. (c) Fine Grid.

Figure 26 : Three grids employed for grid convergence study for shape 32.

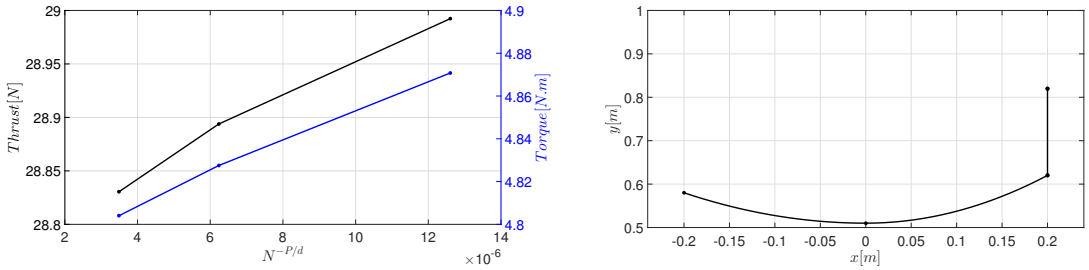

(a) Thrust and torque - Profile 32. (b) Profile 32.

Figure 27 : Grid convergence studies of thrust and torque w.r.t. number of nodes for profile 32.

Verification via Inverse Design I

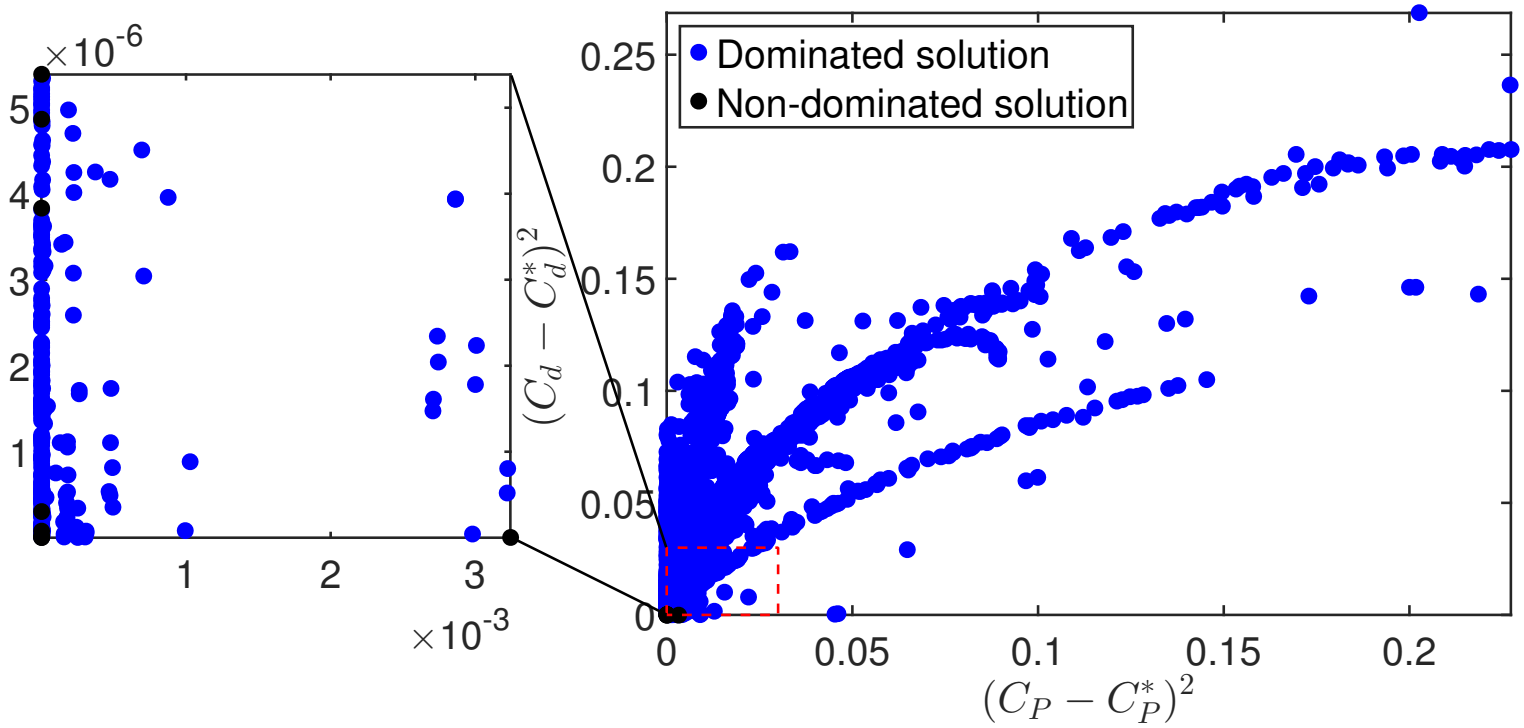

Figure 28 : Dominated and non-dominated solutions of an inverse design simulation.

Verification via Inverse Design II

Table 9 : Comparisons between the target and optimized profiles A, B, and C.

	L_D	h	R_N	L_N	R_D	$\left(C_P - C_P^*\right)^2$	$\left(C_d - C_d^*\right)^2$
Target Profile	0.174	0.02	0.536	0.181	0.604	0	0
Optimized Profile A	0.184	0.137	0.571	0.124	0.571	5.54×10^{-12}	5.39×10^{-06}
Optimized Profile B	0.189	0.046	0.535	0.089	0.587	5.31×10^{-09}	7.73×10^{-08}
Optimized Profile C	0.139	0.063	0.521	0.147	0.558	3.24×10^{-03}	1.72×10^{-10}

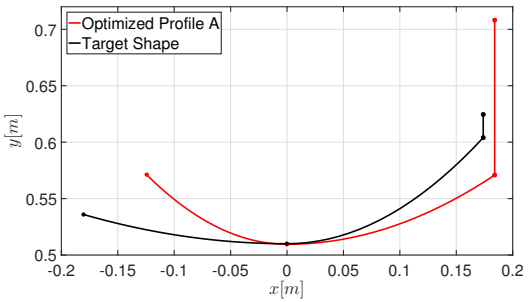

(a) Optimized shape A.

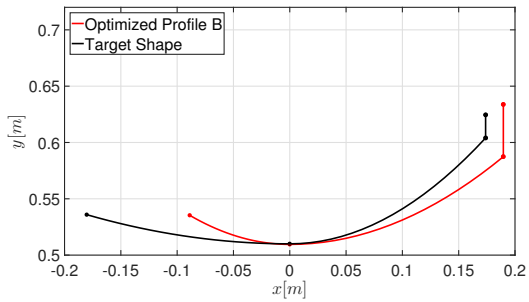

(b) Optimized shape B

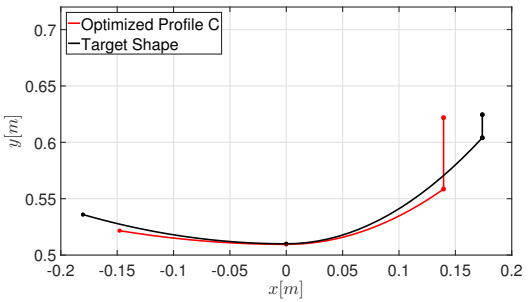

(c) Optimized shape C.

Figure 29 : Inverse design optimized shapes in comparison to target shape.

Shape Optimization Results I

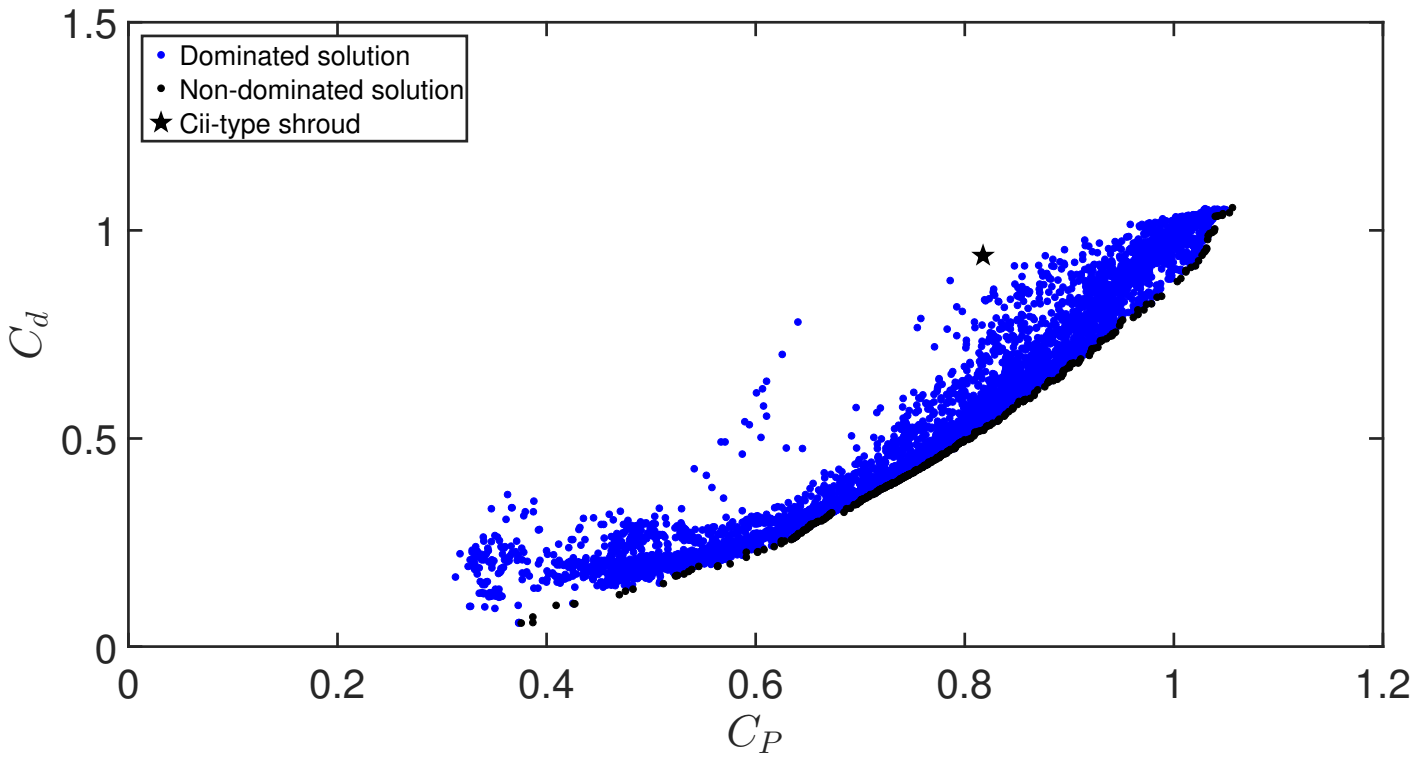

(a) Dominated vs. non-dominated solutions.

Figure 30 : Optimization results.

Shape Optimization Results II

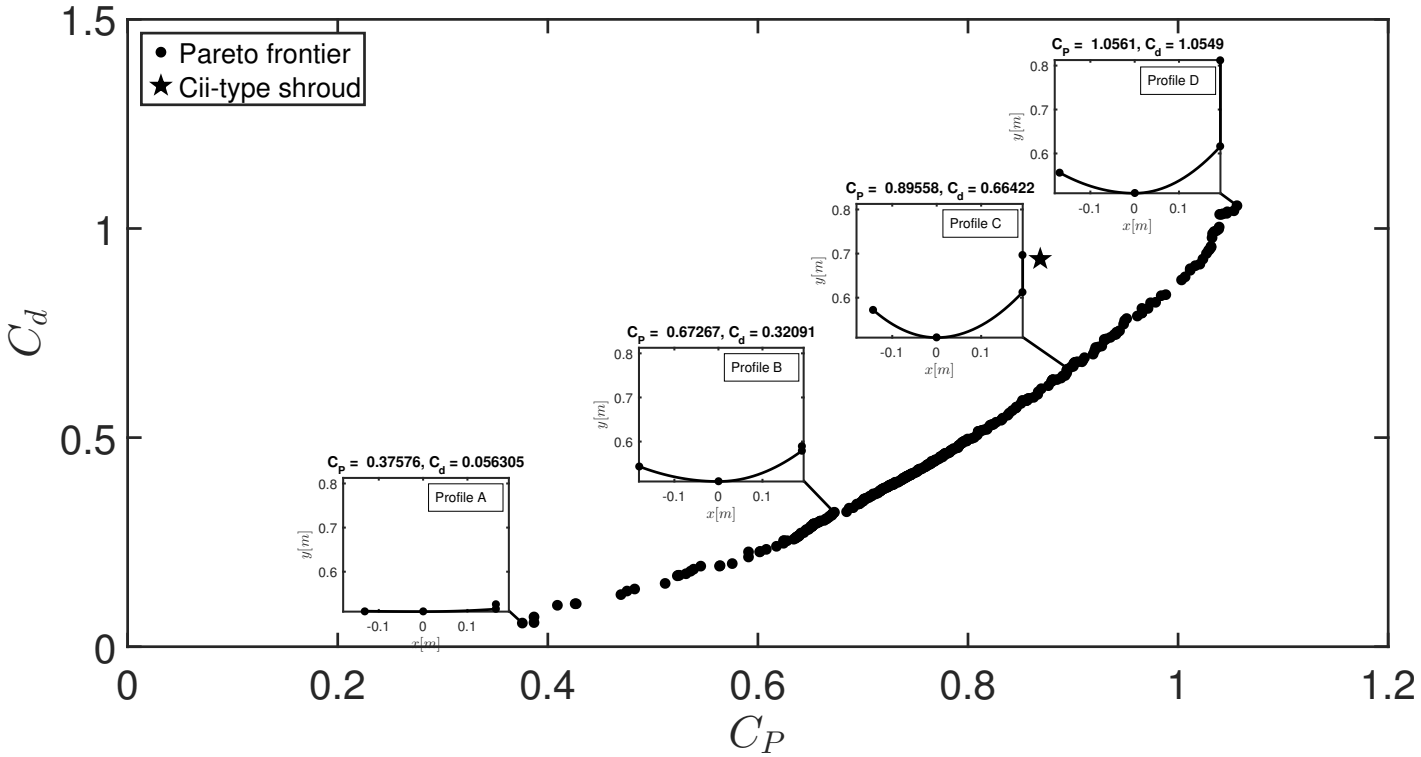

(b) Pareto frontier.

Figure 30 : *Cont.*

Shape Optimization Results III

Table 10 : Comparison between the *Cii* type shroud and optimized profiles C, D, and E.

	L_D	h	R_N	L_N	R_D	C_P	C_d
Cii shroud	0.139	0.102	0.550	0.0897	0.580	0.817	0.939
Profile *C*	0.193	0.084	0.573	0.143	0.613	0.896	0.664
Profile *D*	0.193	0.198	0.557	0.169	0.616	1.056	1.055
Profile *E*	0.193	0.161	0.577	0.176	0.616	1.003	0.876

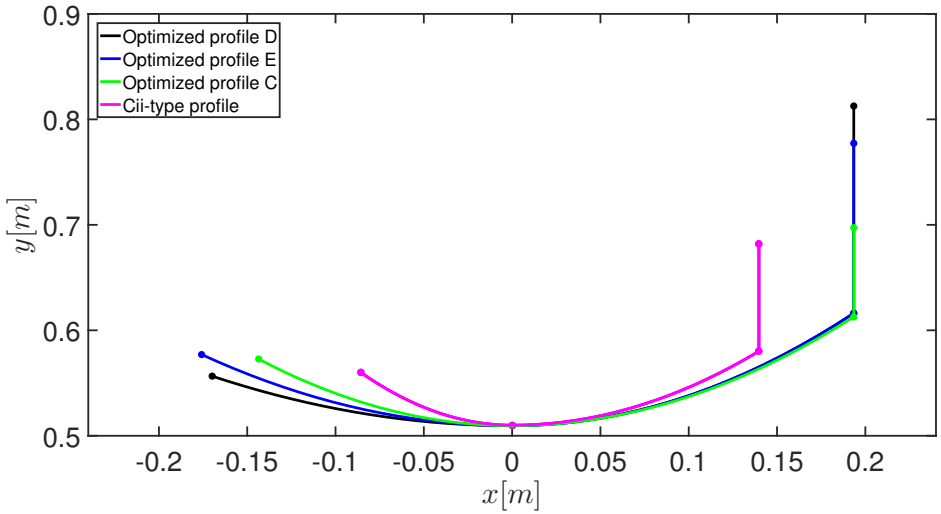

Figure 31 : Selected optimized profiles and baseline shape.

Shape Optimization Results IV

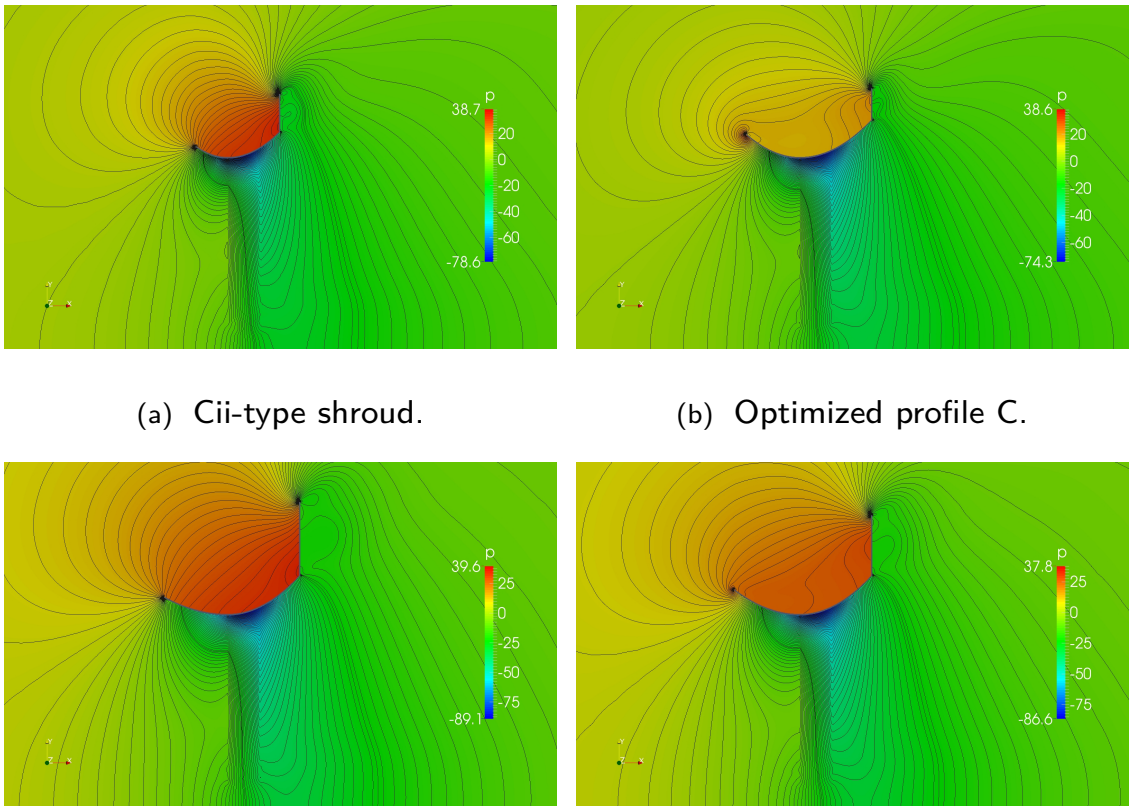

(a) Cii-type shroud.

(b) Optimized profile C.

(c) Optimized profile D.

(d) Optimized profile E.

Figure 32 : Pressure distribution contours for *Cii* profile and optimized profiles C, D, and E.

Shape Optimization Results V

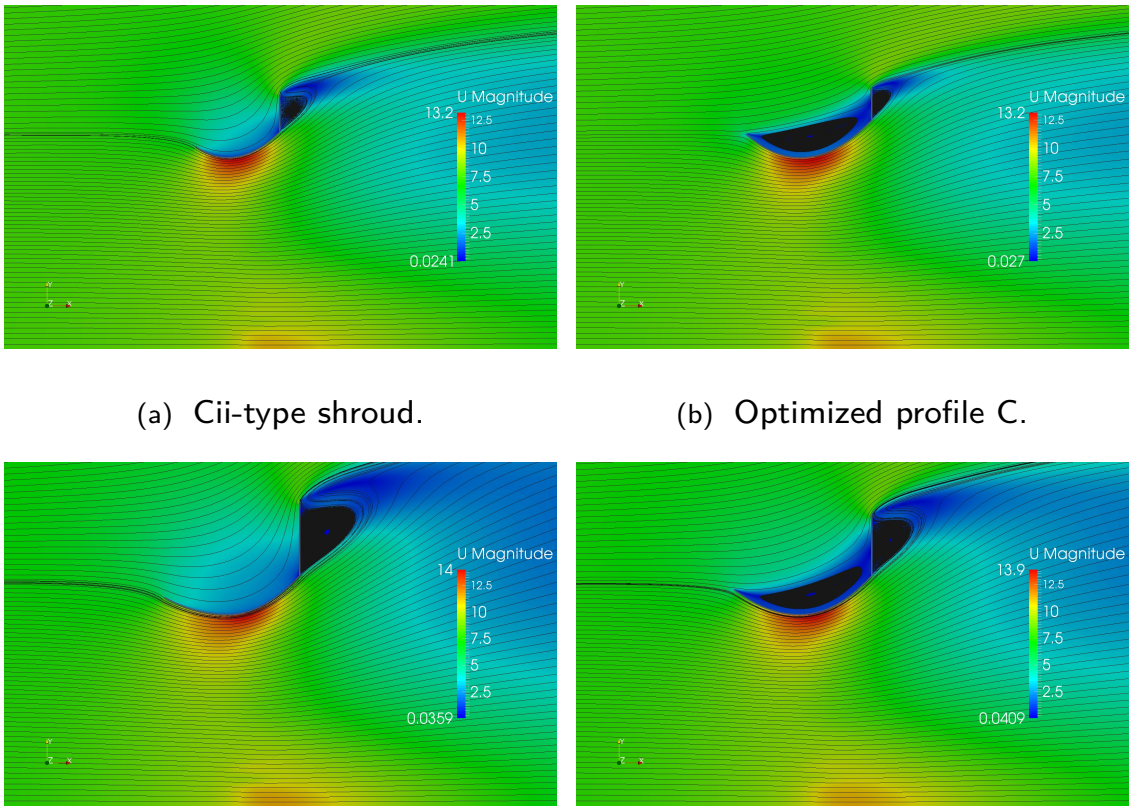

(a) Cii-type shroud.

(b) Optimized profile C.

(c) Optimized profile D.

(d) Optimized profile E.

Figure 33 : Velocity distribution with streamlines for *Cii* profile and optimized profiles C, D, and E.

Conclusion and Future Work

- A framework for the shape optimization of a wind-lens to reduce the drag force and enhance the power production has been presented.
- The shroud of the wind-lens is represented using piece-wise second-order polynomials.
- To determine the power of the shrouded turbine, the RANS equations augmented by a blade element method (BEM) have been employed.
- Further reduction in the computational cost of the simulations is achieved by taking advantage of the axisymmetry of the problem.

Conclusion and Future Work

- The present method has been verified through grid convergence studies and validated by comparisons with wind tunnel test results as well as higher fidelity simulations.
- The axisymmetric RANS-BEM solver has been coupled with DAKOTA's multi-objective genetic algorithm and preliminary results show promise that in fact more optimal shapes than the ones currently used can be found.
- It is likely worthwhile to conduct further investigations by optimizing the profile of the wind-lens as well as the rotor turbine in a combined approach.

Questions?

References

[1] G. Lilley and W. Rainbird, "A preliminary report on the design and performance of ducted windmills," College of Aeronautics Cranfield, Tech. Rep., 1956.

[2] K. Foreman, B. Gilbert, and R. Oman, "Diffuser augmentation of wind turbines," *Solar Energy*, vol. 20, no. 4, pp. 305–311, 1978.

[3] R. Oman, K. Foreman, and B. Gilbert, "A progress report on the diffuser augmented wind turbine," in *Proc. 3rd Biennal Conference and Workshop on Wind Energy Conversion Systems, Washington, DC, USA*, 1975, pp. 819–826.

[4] A. Kogan and A. Seginer, *Shrouded Aerogenerator Design Study: II. Axisymmetrical Shroud Performance*. Technion-Israel Institute of Technology, Department of Aeronautical Engineering, 1963.

[5] O. Igra, "Research and development for shrouded wind turbines," *Energy Conversion and Management*, vol. 21, no. 1, pp. 13–48, 1981.

[6] Y. Ohya, T. Karasudani, A. Sakurai, K.-i. Abe, and M. Inoue, "Development of a shrouded wind turbine with a flanged diffuser," *Journal of wind engineering and industrial aerodynamics*, vol. 96, no. 5, pp. 524–539, 2008.

[7] Y. Ohya and T. Karasudani, "A shrouded wind turbine generating high output power with wind-lens technology," *Energies*, vol. 3, no. 4, pp. 634–649, 2010.

[8] Y. Ohya, T. Uchida, T. Karasudani, M. Hasegawa, and H. Kume, "Numerical studies of flow around a wind turbine equipped with a flanged-diffuser shroud using an actuator-disk model," *Wind Engineering*, vol. 36, no. 4, pp. 455–472, 2012.

[9] L. Tossas and S. Leonardi, "Wind turbine modeling for computational fluid dynamics," *National Renewable Energy Laboratory (NREL), Technical Report No. NREL/SR-5000-55054*, 2013.

References

[10] J. F. Manwell, J. G. McGowan, and A. L. Rogers, *Wind energy explained: theory, design and application*. John Wiley & Sons, 2010.

[11] E. Kulunk, *Aerodynamics of wind turbines*. INTECH Open Access Publisher, 2011.

[12] H. MATSUMIYA, T. KOGAKI, N. TAKAHASHI, M. IIDA, and K. WASEDA, "Development and experimental verification of the new mel airfoil series for wind turbines," *Wind Energy Utilization Symposium*, vol. 22, pp. 92–95, 2000.

[13] M. Berger and Z. Wang, "International journal of computational fluid dynamics," *International Journal of Computational Fluid Dynamics*, vol. 19, no. 8, p. 547, 2005.

[14] B. Adams, M. Ebeida, M. Eldred, J. Jakeman, L. Swiler, A. Stephens, D. Vigil, and T. Wildey, "Sandia technical report sand2014-4633," 2014.

Shape Optimization Results VI

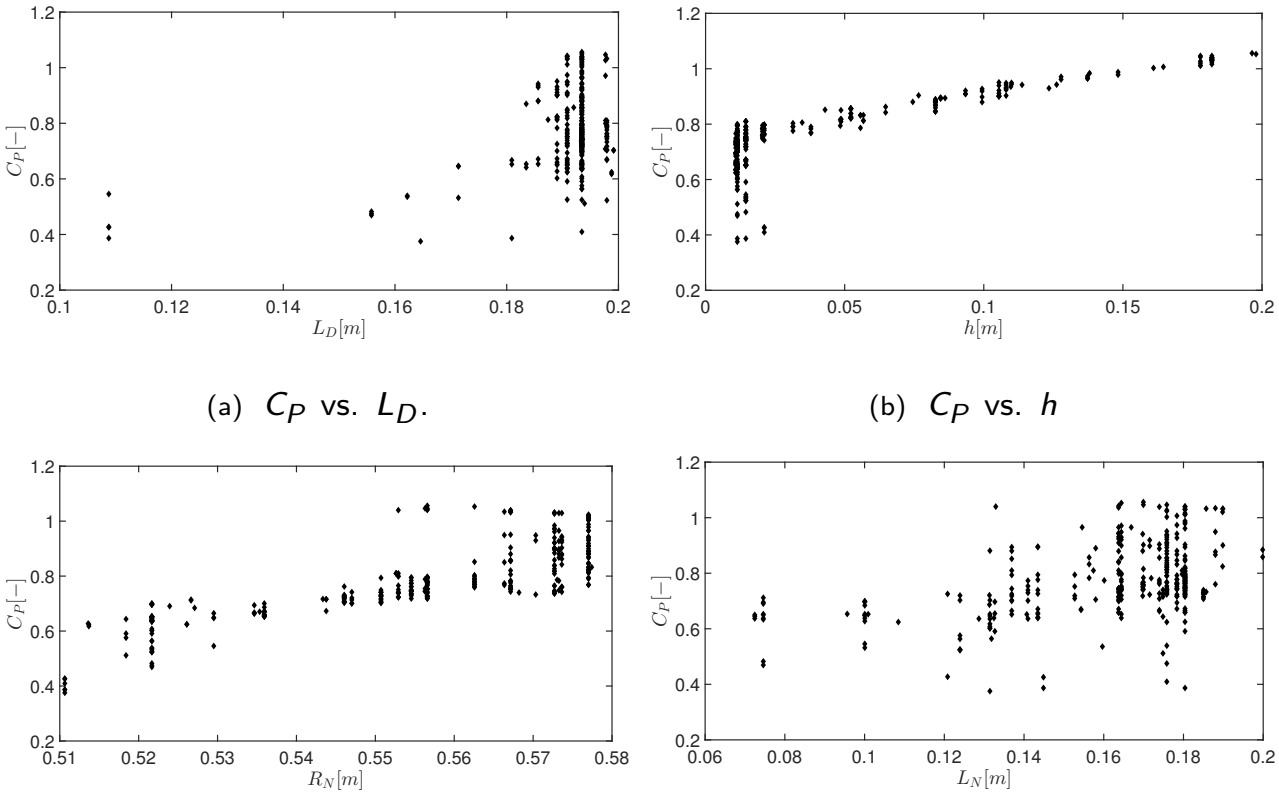

(a) C_P vs. L_D.

(b) C_P vs. h

(c) C_P vs. R_N.

(d) C_P vs. L_N.

Figure 34 : Correlation between the objective function C_P and the design variables in the Pareto Front.

Shape Optimization Results VII

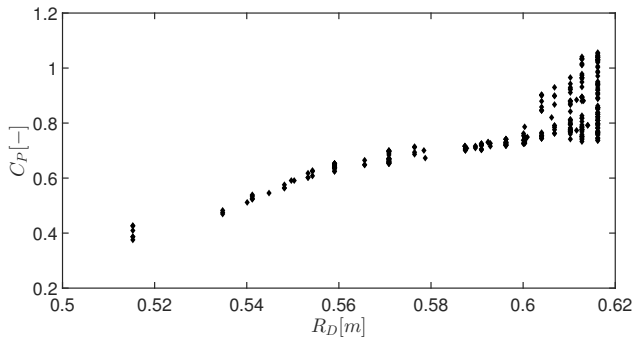

(c) C_P vs. R_D.

Figure 34 : *Cont.*

Discussion

If one normalizes, say optimized profile E, with A_{brim} instead the output power coefficient C_P^{brim} becomes 0.53 instead of 0.896.